Work optimization predicts accretionary faulting: An integration of physical and numerical experiments

Authors
Jessica A. McBeck[1,2], Michele L. Cooke[1], Justin W. Herbert[1], Bertrand Maillot[3], Pauline Souloumiac[3]

Affiliations
1 Department of Geosciences
University of Massachusetts Amherst
Amherst, MA, United States

2 Physics of Geological Processes
University of Oslo
Oslo, Norway

3 Département Géosciences et Environnement
Université de Cergy-Pontoise
Cergy-Pontoise, France

Corresponding author
Jessica A. McBeck
j.a.mcbeck@geo.uio.no

Key points

- Comparison of physical and numerical experiments
- Work optimization prediction closely matches observed
- Work optimization predicts faulting more exactly than max Coulomb stress

McBeck, J., M. L. Cooke, J. Herbert, B. Maillot and P. Souloumniac, (2017) Work optimization predicts accretion faulting: An integration of physical and numerical experiments, *JGR Solid Earth*, 122. doi: 10.1002/2017JB013931.
To view the published open abstract, go to **http://dx.doi.org** and enter the DOI.

Abstract: We employ work optimization to predict the geometry of frontal thrusts at two stages of an evolving physical accretion experiment. Faults that produce the largest gains in efficiency, or change in external work per new fault area, $\Delta W_{ext}/\Delta A$, are considered most likely to develop. The predicted thrust geometry matches within 1 mm of the observed position and within a few degrees of the observed fault dip, for both the first forethrust and backthrust when the observed forethrust is active. The positions of the second backthrust and forethrust that produce >90% of the maximum $\Delta W_{ext}/\Delta A$ also overlap the observed thrusts. The work optimal fault dips are within a few degrees of the faults dips that maximize the average Coulomb stress. Slip gradients along the detachment produce local elevated shear stresses and high strain energy density regions that promote thrust initiation near the detachment. The mechanical efficiency (W_{ext}) of the system decreases at each of the two simulated stages of faulting and resembles the evolution of experimental force. The higher $\Delta W_{ext}/\Delta A$ due to the development of the first pair relative to the second pair indicates that the development of new thrusts may lead to diminishing efficiency gains as the wedge evolves. The numerical estimates of work consumed by fault propagation overlap the range calculated from experimental force data, and crustal faults. The integration of numerical and physical experiments provides a powerful approach that demonstrates the utility of work optimization to predict the development of faults.

Index Terms: 8010 Fractures and faults; 8118 Dynamics and mechanics of faulting (8004); 8170 Subduction zone processes (1031, 3060, 3613, 8413); 8020 Mechanics, theory, and modeling

Keywords: Work optimization, Accretion, Numerical modeling, Analog experiment, Fault development

1. Introduction

Geophysical observations have shed critical insight on the geometry of faults that develop at the front of accretionary wedges [e.g., *Bangs et al.*, 2004; *Barnes et al.*, 2002; *Davey et al.*, 1986; *Gulick et al.*, 2004; *Kopp et al*., 2000; *Moore et al*., 1990]. Balanced restorations of interpretations of fault geometry have constrained the development of these faults [e.g., *Adam et al.*, 2004; *Moore et al.*, 2011; *Morgan and Karig,* 1995; *Nemcok et al.,* 1999]. In complement to these geophysical interpretations, numerical models and scaled analog experiments capture the physics of accretionary faulting and so have lent additional insight into fault mechanics at the deformation front [e.g., *Baba et al.,* 2001; *Buiter*, 2012; *Burbidge & Braun,* 2002; *Del Castello & Cooke,* 2007; *Graveleau et al.,* 2012; *Haq*, 2012; *Konstantinovskaia & Malavielle*, 2005, 2011; *Koyi & Cotton,* 2004; *Malavielle*, 2010; *McClay & Whitehouse*, 2004; *Miyakawa et al.,* 2010; *Mulugeta & Koyi*, 1992; *Naylor et al.,* 2005; *Persson & Sokoutis*, 2002*; Storti & McClay*, 1995]. Many previous studies have predicted the geometry of accretionary faults using the conjugate failure planes that maximize Coulomb stress [e.g., *Mulugeta,* 1988; *Huiqi et al*., 1992], while fewer analyses have predicted this geometry through the optimization of energy components [*Cubas et al*., 2008; *Del Castello & Cooke*, 2007; *Maillot et al*., 2007; *Maillot & Koyi,* 2006; *Mary et al.,* 2013; *Maillot & Leroy,* 2003]. Predictions of accretion thrust geometries using limit analysis, which identifies the active thrust geometry that produces the least upper bound in tectonic force following the maximum strength theorem, closely match thrust geometries observed in physical experiments [*Cubas et al*., 2013; *Mary et al.,* 2013]. In addition, numerical simulations of a physical accretion experiment suggest that the evolution of external work can shed insight on the growth of new accretionary thrusts [*Del Castello & Cooke*, 2007].

Del Castello & Cooke [2007] compare the efficiency of backthrust-forethrust pairs located at two different positions within a simulated accretion experiment, and find that the most efficient pair best matches the position of the observed thrust pair. However, a more complete and systematic search for the most efficient position and dip of thrusts in an evolving physical accretion experiment has yet to be exacted. Additionally, the predictions of work optimization and Coulomb criteria have yet to be systematically compared. To address these gaps, we utilize numerical simulations of a physical accretion experiment to compare the predicted thrusts from external work optimization and Coulomb stress to the observed experimental fault geometries.

We use work optimization to predict the geometry of accretion thrusts that develop in two stages of a physical accretion experiment associated with the development of the first and second backthrust-forethrust pairs. Within the work optimization framework, we predict that the fault configuration that produces the largest gains in the overall system's efficiency, or the change in external work per new fault area, $\Delta W_{ext}/\Delta A$, will develop, rather than less efficient configurations. In order to identify the most efficient fault configuration, we compare $\Delta W_{ext}/\Delta A$ for numerical simulations that include faults at different positions and dips within the accretionary wedge. To assess the utility of the work optimization approach, we compare the geometry of the most efficient faults predicted by work optimization to the geometry observed in the physical experiment and the fault geometry that maximizes Coulomb stress.

2. Growth of faults within accretionary wedges

Predictions of the geometry of accretionary faults using critical Coulomb wedge theory match many geophysical observations [e.g., *Adam & Reuther,* 2000; *Dahlen*, 1984, 1990; *Davis et al.*, 1983; *Davis & von Huene,* 1987; *Kopp & Kukowski*, 2003; *Lallemand et al.*, 1994; *Saffer & Bekins,* 2002; *Zhao et al.,* 1986]. This theory proposes that accretionary systems develop via the propagation of frontal thrusts until the angle between the wedge slope and basal surface attains a critical value [*Dahlen*, 1984; *Dahlen et al*., 1984; *Davis et al*., 1983; *Willette*, 1992; *Yuan et al.*, 2015]. The dips of new accretion thrusts depend on the orientation of the local principal stress, as well as the internal friction of the wedge [*Dahlen*, 1984; *Dahlen et al*., 1984; *Davis et al*., 1983].

Many experimental accretionary systems accommodate deformation via the outboard propagation of forethrusts [e.g., *Graveleau et al.,* 2012 and references therein] and to the first-order follow critical Coulomb wedge theory. Transient deviations from the steady-state behavior of critical Coulomb wedges have been demonstrated in many physical experiments where accretionary systems evolve through episodic cycles of 1) underthrusting, which causes wedge thickening via slip along existing thrusts, and 2) frontal accretion, which causes wedge lengthening via new accretionary faulting at the front of the wedge [e.g., *Bigi et al*., 2010; *Buiter*, 2012; *Graveleau et al.,* 2012; *Gutscher et al*., 1996, 1998; *Haq*, 2012; *Konstantinovskaia & Malavielle*, 2005; *Malavielle*, 2010; *McClay & Whitehouse*, 2004; *Morgan,* 2015; *Mulugeta & Koyi*, 1992; *Storti & McClay*, 1995]. Additionally, numerical models of accretionary systems [e.g., *Burbidge & Braun*, 2002; *Ellis et al*., 1999, 2004; *Wenk & Huhn*, 2013; *Yamada et al.,* 2014] and interpretations of crustal accretionary wedges [e.g., *Byrne & Fisher,* 1987; *Gutscher et al*., 1996; *Lallemand et al*., 1994; *Moore et al*., 1991; *Takami & Itaya,* 1996; *von Huene & Scholl*, 1991] suggest that accretionary systems develop faults through discrete, transient processes.

The episodic deviations from critical Coulomb wedge theory have been explored by analyzing components of the system's energy budget [e.g., *Burbridge & Braun,* 2002; *Cubas et al.*, 2008; *Del Castello & Cooke*, 2007; *Gutscher et al.,* 1998; *Hardy et al.*, 1998; *Mary et al*., 2013; *Souloumiac et al.*, 2009; 2010; *Yagupsky et al*., 2014]. These analyses have successfully used work optimization to predict the temporal evolution of accretionary systems, including the periodicity of the accretion-underthrusting cycle observed in analog experiments and inferred from seismic images of crustal accretionary wedges [e.g., *Gutscher et al*., 1998; *Burbridge & Braun*, 2002], and the outboard propagation of frontal accretionary faults [*Hardy et al*., 1998]. Other analyses have used energetics to predict the spatial distribution and geometry of accretionary faults [e.g., *Cubas et al*., 2008; *Maillot et al*., 2007; *Maillot & Koyi,* 2006; *Del Castello & Cooke*, 2007; *Mary et al.,* 2013; *Yagupsky et al.*, 2014]. For example, *Mary et al.* [2013] use limit analysis to show that episodic accretion may be linked to slip weakening of the active faults.

Del Castello & Cooke [2007] use the complete deformational work budget to shed insight on the transition from underthrusting to frontal accretion. They show that the external work of the accretionary system decreases with accretionary thrust fault growth as the system becomes more efficient. The complete deformational work budget includes the energy dissipated in internal strain or internal work of deformation, work of uplift against gravity, work done against frictional sliding on faults, energy required to created new fault area, and energy of ground shaking [e.g., *Cooke & Madden*, 2014]. Following the law of conservation of energy, the work consumed in the system must equal the total external work done on the boundaries of the system, W_{ext}. In a two-dimensional system, W_{ext} may be calculated from the sum of the products of shear traction and displacement, τ and u_s, and normal traction and displacement, σ_n and u_n, integrated over all of the model boundaries, B:

$$W_{ext} = \frac{1}{2}\iint_B (\tau u_s + u_n \sigma_n)\, dB \qquad \text{Eq. 1}$$

Within the work optimization framework, fault configurations that produce the maximum gain in W_{ext} per new fault area propagated, $\Delta W_{ext}/\Delta A$, are considered more likely to develop than less efficient fault configurations that produce less $\Delta W_{ext}/\Delta A$ [*Cooke & Madden*, 2014; *McBeck et al.*, 2016]. This method provides a global approach for predicting fault geometry that assesses changes in the stress and displacement fields far from the newly propagated fault, and includes the contribution of all of the deformational processes that consume or produce work within the fault system (Eq. 1) [*Cooke & Madden*, 2014].

3. Methods

To assess the utility of the work optimization approach using numerical simulations of fault growth within a physical accretion experiment, we compare the geometry of the most efficient faults predicted by work optimization to the geometry observed in the physical experiment, and the geometries predicted by Coulomb stress. We numerically simulate two stages of new fault growth observed in a physical accretion experiment (E240) performed at the Université de Cergy-Pontoise (UCP) tectonic modeling lab, and described in *Herbert et al.* [2015].

For this study, we investigate the two stages of the experiment where two new thrusts develop within forethrust-backthrust pairs. We focus on these two stages (first pair and second pair), and not on the intervening stages of single forethrust and backthrust growth, because at these stages of the experiment, the wedge undergoes the most significant reorganizations in active fault configuration with the development of and slip along two new thrust faults. Additionally, searching for the optimal geometry of thrusts in the second backthrust-forethrust pair provides insights into the tradeoffs of continued slip along pre-existing faults versus the propagation of new thrusts. The supplemental text and animations of the strain evolution of the experiment describe in more detail each faulting event in this experiment.

3.1. Physical experiment set up and analysis

For the accretionary experiment E240 performed at UCP, dry sand was deformed in a rectangular box with a fixed frontwall, basal plate and sidewalls [*Herbert et al.*, 2015]. To simulate accretion, an electric screw motor translates the backwall of the box towards the frontwall at a constant speed (0.22 mm/s). Throughout the duration of the experiment, a camera captures photos of the cross section of the wedge through the box's glass sidewall every five seconds, or every 1.1 mm of applied backwall displacement. To construct the sandpack, a sedimentation device, designed and built at UCP, sieves the sand two or three times before deposition [*Maillot*, 2013]. We use the sedimentation device to build a rectangular sandpack (16 mm thick, 41 cm long, 28 cm wide), and an overlying protowedge adjacent to the backwall, which has a slope at the angle of repose of the material, and focuses deformation away from the backwall [*Herbert et al.,* 2015]. The sand deposition method strongly controls the frictional properties of the system, and thus how the sandpack accommodates strain [e.g., *Krantz,* 1991; *Lohrmann et al.,* 2003; *Maillot*, 2013]. The UCP sedimentation device produces homogeneous, isotropic and dense sandpacks consisting of planar sand layers [*Maillot*, 2013]. This homogeneous sandpack enables robust comparison of the thrust geometry observed in the physical experiment and the geometry predicted in the numerical analysis.

We calculate the incremental displacement field of the wedge cross-section with digital image correlation (DIC) of sequential photos captured of the experiment. For every two sequential photos of the wedge cross-section (1.1 mm of shortening) we use Particle Image Velocimetry analysis to determine the instantaneous velocity field at a grid of points through the DIC of pixel constellations [e.g., *Adam et al*., 2005; *Hoth*, 2005]. The velocity fields produced in this DIC analysis do not indicate the velocity of individual grains, but rather groups of neighboring grains that are recognized by similar patterns in sequential images. In order to highlight the rotation of material that indicates the development of discrete thrusts, we use the velocity field to calculate the incremental angular shear strain rate field between successive images. High angular shear strain rates (e.g., curl of velocity field) highlight localized slip along faults. We calculate the angular shear strain rate field of the velocity field, *U*, from the cross product of the gradient operator with the velocity vector, *U*:

$$\nabla x U = \left(\frac{\partial U_y}{\partial x} - \frac{\partial U_x}{\partial y}\right)\hat{z} \qquad \text{Eq. 2}$$

where *x* is the horizontal direction, *y* is the vertical direction, and *z* is the out-of-plane direction.

The incremental horizontal displacement and angular shear strain fields reveal the geometry of the first and second backthrust-forethrust pairs, which meet the base of the experiment at 65±7 mm and 114±6 mm, respectively, from the physical backwall (Fig. 1). The thrust faults are

Figure 1

Strain localization revealed by DIC analysis of physical experiment. Horizontal incremental displacement field (mm) calculated from DIC increments immediately before (A), immediately after (B), and shortly after (C) first backthrust-forethrust pair is observed. Horizontal incremental displacement field calculated in DIC increments immediately before (D), immediately after (E), and shortly after (F) second backthrust-forethrust pair is observed. Angular shear strain rate field (i.e., curl, rad/5s) (G-L) derived from incremental displacement fields. Black lines show numerical model boundaries. After both stages of new thrust pair development, the forethrust has more localized strain than the backthrust.

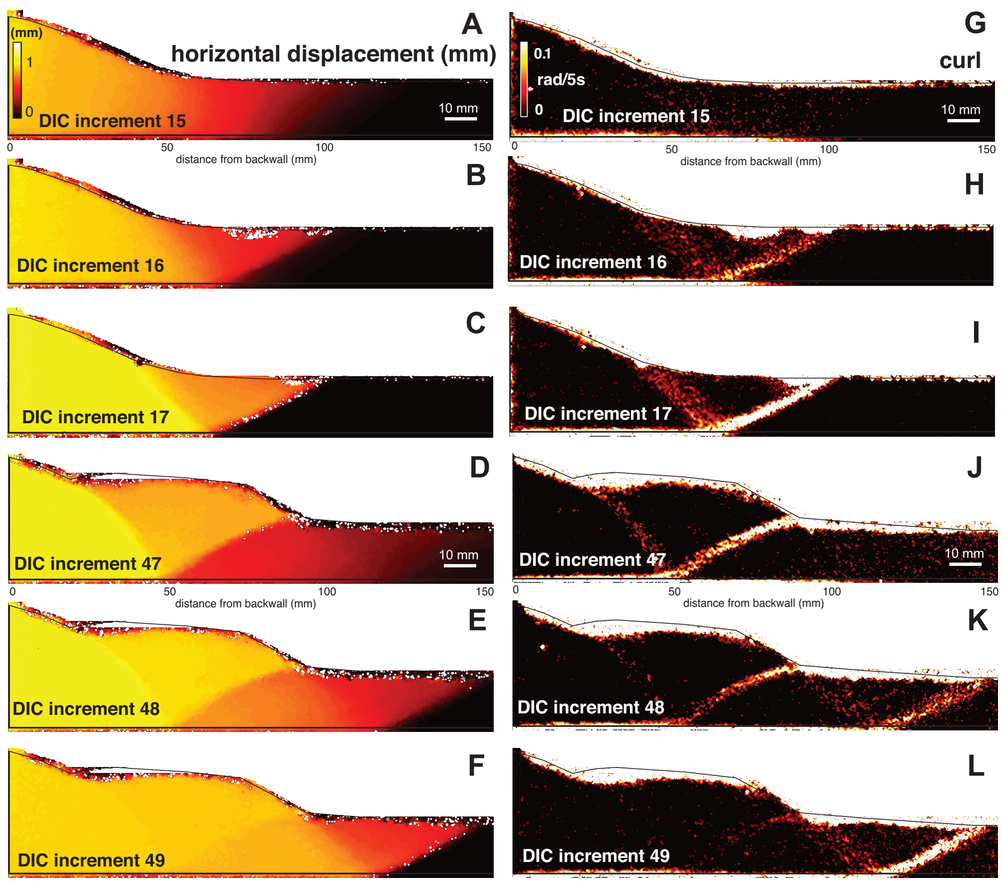

illuminated by both sharp gradients in the horizontal velocity (or incremental displacement) field and by elevated regions of angular shear strain rates (curl rate). The reported range in observed positions of the thrusts arises from the width of regions of elevated angular shear strain rate (Fig. 1, Fig. S1). The width of each thrust fault determined from the angular shear strain rate fields (>1 mm) is larger than the spatial resolution of the DIC analysis (0.38 mm), and indicates a zone of localized shear surrounding each fault. We observe the development of the first and second backthrust-forethrust pairs after about 3 mm and 37 mm of backwall displacement, which are captured in the 16th and 48th incremental displacement fields.

3.2. Development of numerical simulation of the physical experiment

We simulate the UCP accretion experiment with the two-dimensional, plane strain, linear elastic, Boundary Element Method (BEM) modeling tool Fric2D [*Cooke & Pollard*, 1997]. Fric2D solves the quasi-static equations of deformation to determine the displacements and tractions on each element and at specified points within the model, produced by a given set of boundary conditions and fracture geometry [e.g., *Cooke & Pollard*, 1997; *Cooke & Murphy,* 2004; *Cooke & Madden,* 2014]. The BEM approach of Fric2D only requires the discretization of fractures and boundaries, which are comprised of linear elements that may not interpenetrate. Additionally, Fric2D 3.2.7 can simulate slip-weakening behavior along pre-existing fractures and/or potential growth elements [*Savage & Cooke*, 2010]. When an element slips beyond a prescribed slip-weakening distance, the coefficient of friction along that element evolves linearly from its static to its sliding value.

The Fric2D numerical models employed here simulate increments of deformation associated with two stages of thrust development in the experiment. The two-dimensional models replicate the cross section of the physical wedge observed through the glass sidewalls. The deformation captured in one increment of the DIC analysis determines the distribution of displacements applied to the model boundaries. To simulate the increments of deformation, we derive the incremental horizontal and vertical displacements observed along the moving backwall and just above the base of the experiment near the physical detachment, and apply these displacements to the corresponding boundaries of the numerical model. In this process, we first calculate the incremental displacement field using DIC of sequential photos before the first and second backthrust-forethrust pairs form (Fig. 1). Next, we extract a transect of the horizontal and vertical components of the incremental displacement field 1.42 and 1.21 mm above the base of the model, for the first and second stages of faulting, respectively (Fig. 2A-D). We select a transect depth that is close to the sliding detachment fault along the base of the model (Fig. 1), but avoids significant artifacts in the DIC data that occur along the base of the sandpack. To reduce noise in the incremental displacements, we run a fifteen-point median filter on the raw displacements in order to remove outliers. Then we calculate the five-point central moving average of the filtered displacements, which reduces noise with wavelengths less than two millimeters and preserves larger scale fluctuations in the displacements (Fig. 2E-F).

This incremental displacement applied to the numerical model boundaries represents the deformation associated with slip along the basal detachment of the physical experiment. Consequently, these models do not explicitly simulate detachment deformation via slip along a frictional fault. However, the frictional work of the experimental detachment is captured in the modeled external work because the total external work on the numerical model is comprised of the work done on the backwall, as well as that done on the basal boundary, which simulates the detachment deformation.

For this investigation, the displacements applied to the boundaries of the numerical model should be sufficiently large to produce slip along all of the contender faults investigated, but sufficiently small to reduce distortion of the elements. Because Fric2D employs Eulerian deformation, the maximum boundary displacement should be less than half of the element size, which for these models is 1 mm. Consequently, the smoothed incremental displacements observed in the physical experiments are scaled by approximately one-half so that the maximum horizontal displacement is 0.50 mm. Using larger elements could permit the application of larger horizontal displacements, but has the undesirable effects of decreasing both the resolution and accuracy of the numerical solution. As long as the increment of displacement is sufficiently large to cause frictional slip along all of the potential faults within the model, then the relative efficiency of each thrust geometry remains unchanged regardless of the magnitude of applied displacements. Consequently, the optimal thrust geometry does not depend on the magnitude of the applied displacements. For these numerical simulations, the scaled displacements are sufficient to cause slip along faults that dip within 20° of the observed thrusts and are located within 30 mm of the observed thrusts, allowing assessment of the gain in efficiency of a broad

Figure 2: Boundary conditions of models are determined from DIC of physical experiment. Horizontal incremental displacement field immediately preceding development of first (A) and second (B) backthrust-forethrust pair. Horizontal black line shows location of transect that samples displacement field near physical detachment. Vertical incremental displacement field immediately preceding development of first (C) and second (D) backthrust-forethrust pair. Horizontal and vertical incremental displacements along transect near base of physical experiment for first (E) and second (F) stages of faulting. Blue dots show raw displacements calculated with DIC analysis. Red dots show displacements after median filter performed. Dark blue lines show smoothed displacements. Light blue lines show filtered, smoothed, scaled displacements, in which the maximum horizontal displacement is 0.5 mm. Numerical model boundaries and displacement loading conditions for first (G) and second (H) stages of faulting. Coordinate system of loading conditions is relative to boundary elements, and shown with gray arrows (G). Horizontal displacement field within numerical simulations of first (I) and second (J) stages of faulting. Rightward displacements are positive. Vertical displacement field within numerical simulations of first (K) and second (L) stages of faulting. Upward displacements are positive.

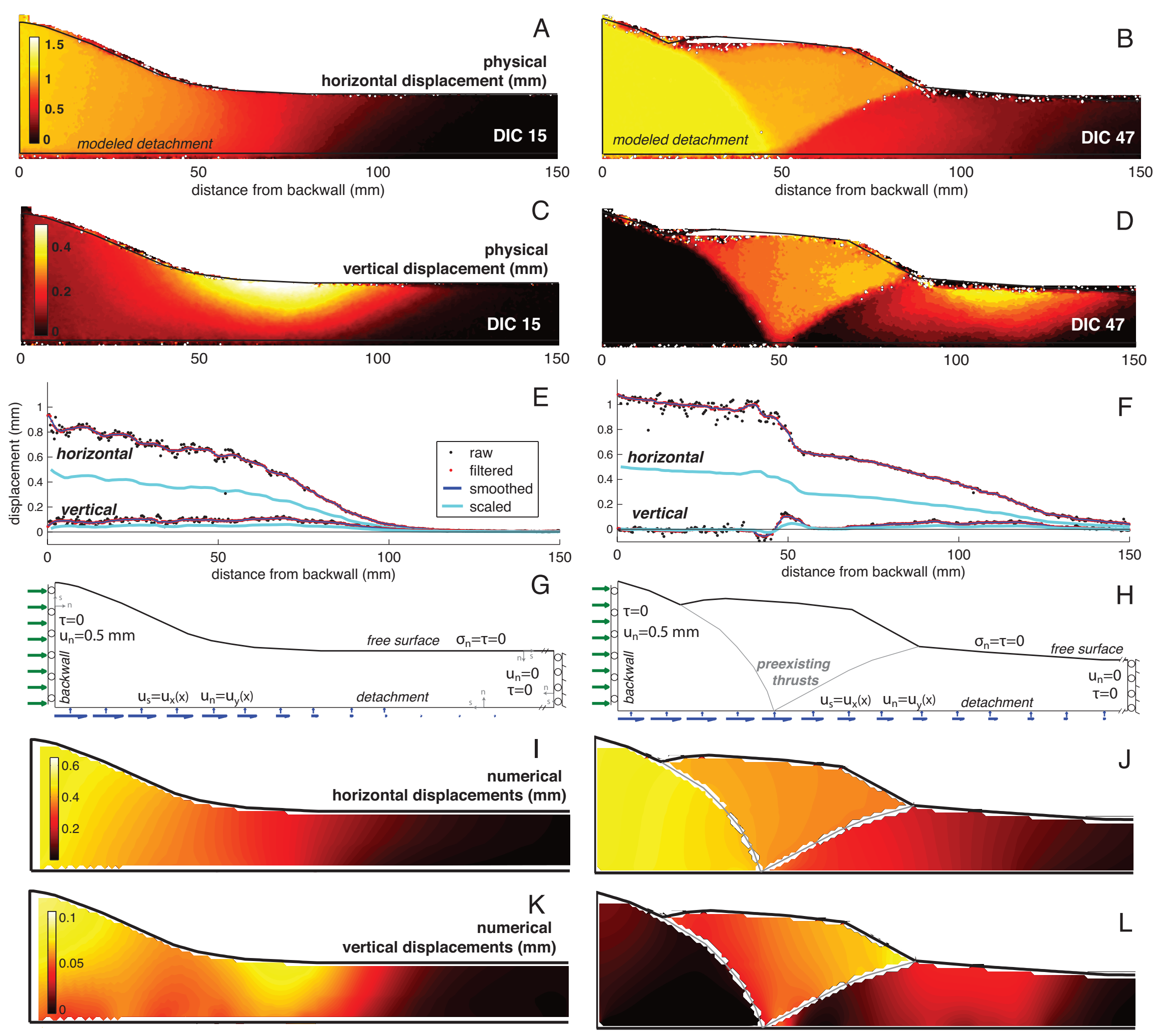

range of fault geometries. The vertical displacements are scaled by the same ratio as the horizontal displacements.

Along each model boundary, we prescribe either displacements or tractions for the normal and shear components of the boundary conditions, and Fri2D solves for the unprescribed displacements or tractions. We apply the maximum basal horizontal displacement (0.5 mm) as the rightward normal displacement, u_n, on the left model boundary to simulate the translation of the backwall (Fig. 2D). We set shear tractions, τ=0, on this boundary, so that it is free to displace vertically. We prescribe zero normal displacements, u_n=0, and shear tractions, τ=0, to the rightmost model boundary so that it does not translate horizontally. Allowing the left and right model boundaries to displace vertically enables the thickening of the sandpack near the backwall, such as observed in this physical experiment, as well as other physical accretion experiments [e.g., *Souloumiac et al.*, 2010]. We allow the top boundary of the model (i.e., the topography of the experimental wedge) to deform freely, such that this boundary experiences zero normal and shear tractions, σ_n=τ=0. We use the topography of the physical wedge at the two stages of interest within the experiment as the geometry of the top boundary of the models.

Boundaries with zero-valued components of either applied tractions or displacement do not contribute to the external work (Eq. 1). Consequently, the external work of these accretion models depends on the resulting normal tractions on the left side of the model, the modeled moving backwall, B_a, as well as the shear and normal tractions along the base of the model, the modeled detachment, D, so that Eq. 1 may be expressed as

$$W_{ext} = \frac{1}{2}\iint_D \left(\tau u_s + u_n\sigma_n\right) dD + \frac{1}{2}\iint_{B_a}(u_n\sigma_n)\, dB_a \qquad \text{Eq. 3}$$

Measurements of the dry CV32 sand used in the experiment constrain the material and fault properties (i.e., Young's modulus, density, static and dynamic friction) of the models [e.g., *Cubas et al*., 2010; *Herbert,* 2014; *Lambe and Whitman*, 1969; *Maillot*, 2013]. Table 1 lists the intact material and fault properties used in the models simulating the physical experiments. Although the choice of material properties can change the threshold conditions for the onset of failure, they do not influence the determination of the most efficient fault geometry. Varying the material parameters may change the value of W_{ext} for the simulations, but will not significantly alter the distribution of ΔW_{ext} among the faults that fail. We load the models so that many

Table 1: Intact material and fault properties of numerical simulations.

Property	Value
Poisson's ratio	0.2
Young's modulus	0.25 MPa
Mode-I fracture toughness	2.5 MPa*m$^{1/2}$
Density	1700 kg/m^3
Cohesion	0 MPa
Static friction coefficient	0.65
Dynamic friction coefficient	0.17
Slip-weakening distance	0.25 mm

Intact and fault properties used in numerical models. Intact properties are representative of CV32 sand used at UCP [*Herbert et al*., 2015; *Maillot,* 2013]. Poisson's ratio value is typical for dry sand [e.g., *Lambe and Whitman*, 1969]. Sandpacks constructed with UCP sedimentation device produce uniform sandpacks with density of 1700 kg/m^3 [*Cubas et al*., 2010; *Maillot*, 2013]. Young's modulus is calculated from force measurements on backwall of experimental device [*Herbert*, 2014]. Casagrande shear box tests determine an intact coefficient of friction of 0.96 and dynamic friction of 0.72 [*Maillot*, 2013]. Friction coefficients slightly below these values are used in order to represent failure along more evolved failure surfaces that include sand grains that are more favorably aligned for slip. The chosen slip-weakening distance matches the median diameter of the CV32 sand grains.

potential faults fail, and then we investigate their relative impact on ΔW_{ext}. Because we load the system well beyond the threshold conditions for the onset of faulting, the specific values for boundary displacement and material properties, which control the failure threshold, do not impact the assessment of the optimal fault geometry. This approach of loading the system beyond the threshold for failure is more computationally efficient than investigating all potential faults with successive monotonic loading steps up to the threshold conditions for failure for each fault.

The applied loading conditions, material properties, and wedge geometry produce displacement fields within the numerical simulation (Fig. 2I-L) that share first-order patterns with the observed displacement fields (Fig. 2A-D). In the first stage of faulting, the incremental horizontal displacements of the physical experiment (Fig. 2A), and within the numerical simulation (Fig. 2I), gradually decrease with distance from the backwall. The incremental vertical displacements show a wide region of uplift from about 50-100 mm from the backwall in both the physical experiment (Fig. 2C) and the simulation (Fig. 2K). In the second stage of faulting, the simulation produces a horizontal displacement field that is very similar to the observed displacement field. The regions of the wedge between the pre-existing thrusts, and between the backwall and the pre-existing backthrust, move to the right as relatively coherent blocks without significant horizontal compaction (i.e., without large gradients in horizontal displacement) (Fig. 2B, J). Additionally, the horizontal displacements within the portion of the wedge outboard of the pre-existing forethrust gradually decrease with increasing distance from the backwall, indicating compaction (Fig. 2B, J). Furthermore, the simulation produces a broad region of uplift extending from about 80-120 mm from the backwall (Fig. 2L) that matches the region of diffuse incremental vertical uplift that occurs outboard of the pre-existing pair within the physical experiment (Fig. 2D). In both the numerical simulation and the physical experiment, vertical uplift is greatest within the wedge between the pre-existing thrust faults.

3.3. Work optimization approach

To investigate the impact of accretionary faulting on the mechanical efficiency of the accretionary wedge, we calculate the change in external work per fault area, $\Delta W_{ext}/\Delta A$, produced by new faults at systematically varying positions and dips within the wedge. The fault geometry that produces the largest $\Delta W_{ext}/\Delta A$ is considered the most efficient, and thus most likely to develop according to work optimization principles [e.g., *Cooke & Madden*, 2014]. We use the ratio $\Delta W_{ext}/\Delta A$ to determine the most efficient geometry because faults with longer lengths, and thus larger areas, can accommodate more slip and so produce greater ΔW_{ext} than shorter faults [e.g., *Cooke & Madden*, 2014; *McBeck et al*., 2016]. While the growth of longer faults results in more efficient systems, the growth of these faults also consumes greater work in the production of new fault surface area [e.g., *Chester et al*., 2005; *Wilson et al*., 2005; *Herbert et al*., 2015]. The reported gain in efficiency indicates the increase in system efficiency (ΔW_{ext}) per change in fault area, ΔA. Consequently, $\Delta W_{ext}/\Delta A$ reveals fault geometries that are efficient relative to the cost of propagating new fault area. We calculate fault area from simulated fault length as Fric2D simulates a 2D, plane strain environment in which the model is one unit thick in the z-direction. For the analysis employed here, the change in fault area, ΔA, is the difference in total fault area following the addition of a new fault to the model, which is the area of the newly added fault.

We compare the efficiency of one new fault at a time within the two stages of wedge development in which the first and second backthrust-forethrust pairs form. The modeled faults root at the model base and intersect the top boundary of the model in a similar manner to the observed faults in the physical experiments. In the first stage of fault growth investigated, we predict the geometry of thrusts in the first backthrust-forethrust pair. In the second stage of fault growth investigated, we predict the geometry of the second backthrust-forethrust pair and investigate the influence of the new fault geometry on system efficiency that contains pre-existing faults, which accommodate slip before the second pair develops (Fig.1).

In the analysis of the first stage of thrust faulting, we vary the position and orientation of each new fault and calculate the $\Delta W_{ext}/\Delta A$ due to faults that root at the model base from 49 to 111 mm from the backwall, in increments of 2 mm, and orientations from 20° to 170° in increments of 2°. Reported positions are measured as the horizontal distance from the backwall to the intersection of the thrust root with the base of the model. Reported orientations are measured clockwise from the left horizontal. With this sign convention and model design, faults oriented 0-90° are backthrusts, and 90-180° are forethrusts. The tested range of fault positions and orientations includes the approximate positions of the backthrust (65±7 mm) and forethrust (65±5 mm), and dips of the backthrust (45±10°) and forethrust (156±4°) observed in the physical experiment (Fig. S1). In the analysis of the second stage of thrust faulting, we vary the position of faults from 80 to 138 mm from the backwall, in increments of 2 mm, and the orientations from

Figure 4

Comparison of observed thrusts to efficient thrusts for first (A-B) and second (C-D) stages of faulting. Regions of high curl indicate localization of angular shear strain along faults. A, C) Location of most efficient backthrust (thickest line), extent of backthrusts that produce >90% of the maximum $\Delta W_{ext}/\Delta A$ (thinner lines), and extent of backthrusts that produce >80% of the maximum $\Delta W_{ext}/\Delta A$ (thinnest lines). B, D) Locations of efficient forethrusts. The backthrust geometries that produce >80% of the maximum $\Delta W_{ext}/\Delta A$ overlap regions of high curl along the observed backthrust in the first and second stages of faulting (A,C). The forethrust geometries that produce >90% of the maximum $\Delta W_{ext}/\Delta A$ overlap regions of high curl along the observed forethrust in the first and second stages of faulting (B,D).

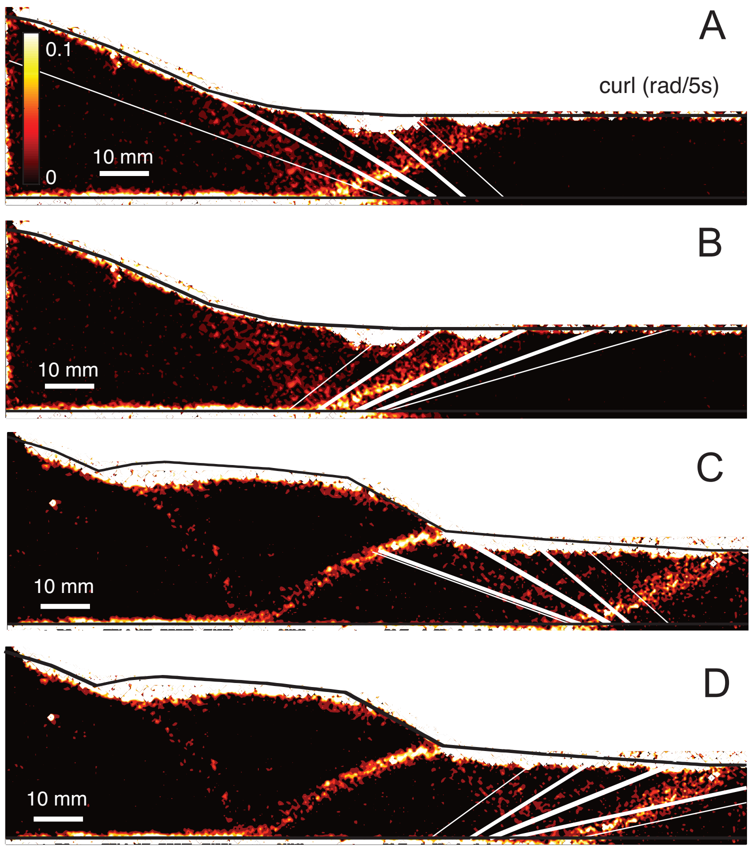

20° to 170°, in increments of 2°. These ranges include the approximate observed positions of the backthrust (114±6 mm) and forethrust (114±5 mm), and orientations of the backthrust (38±5°) and forethrust (156±3°) (Fig. S1).

For some of the fault geometries tested in the second stage analysis, the added fault intersects the pre-existing forethrust. In these scenarios, we shorten the new fault so that it ends at the pre-existing forethrust. We assume that if a new fault intersects the pre-existing forethrust, the most efficient fault will terminate at the thrust. In the physical experiment, the second forethrust-backthrust pair does not intersect the pre-existing forethrust. Consequently, in this analysis, we presume that the thrusts that maximize $\Delta W_{ext}/\Delta A$ will form sufficiently outboard of the pre-existing thrusts such that they do not intersect or terminate at the pre-existing forethrust.

3.4. Coulomb stress analysis

To evaluate the utility of the work optimization approach relative to traditional fault predictions, we compare the orientation of the most efficient faults to the orientations of fault planes that maximize Coulomb stress. We calculate the Coulomb stress at each element of each potential fault over a range of dips at the position that matches the observed fault geometry. Using a tension positive sign convention, Coulomb stress, S_c, may be calculated from the shear traction, τ, the coefficient of internal friction, μ, and the normal traction, σ_n, as

$$S_c = |\tau| + \mu\sigma_n \qquad \text{Eq. 4}$$

In order to calculate Coulomb stress, we find the shear and normal tractions along elements of potential fault planes prior to any slip or opening along those elements. Coulomb shear failure of those planes occurs when the Coulomb stress exceeds the inherent shear strength of the material. In this comparison of Coulomb stress and work optimization, we load the numerical models beyond the threshold conditions for failure such that a range of potential fault plane orientations fail in shear, and assess the relative Coulomb stress along the potential faults. This approach follows that for identifying the faults that optimize $\Delta W_{ext}/\Delta A$.

To compare the orientations of planes that maximize Coulomb stress with the work optimization predictions, we calculate both the average and maximum Coulomb stress along modeled faults prior to slip along those faults. In this comparison of Coulomb stress and work optimization predictions, faults that produce high $\Delta W_{ext}/\Delta A$ are considered more likely to develop than less efficient faults, and planes with high Coulomb stress are considered more likely to fail than planes with lower stress.

4. Results

We present the results of this work optimization analysis by first comparing the analyses of the first stage of faulting to the second stage. Then we compare the numerical predictions of highly efficient faults to the fault geometries observed in the physical experiment. Following these investigations, we search for the most efficient backthrust geometry in a system that includes the observed forethrust geometry. Next we compare the highly efficient fault geometries to the fault dips predicted by Coulomb stress. To shed insight on the evolution of system efficiency throughout accretion, we track the external work of numerical systems with fault geometries that match geometries observed in stages of the physical experiments.

4.1. Comparison of first and second stages of faulting

Systematic investigation of external work for a wide range of single fault position and dip reveals that both stages of accretion produce two highly efficient thrust geometries: one forethrust and one backthrust for each stage (Fig. 3). To assess these model results, we remove results from the search for the most efficient thrust geometry that have anomalously high condition numbers that exceed 125% of the mode (Fig. S2). The condition numbers of BEM influence coefficients relate the displacements and tractions of each element on every other element in the model [e.g., *Cooke and Pollard*, 1997], and indicate the relative robustness of the matrix inversions [e.g., *Knupp*, 2000], which vary when element nodes are too closely spaced or element sizes are irregular. In this study, models with high condition numbers produce $\Delta W_{ext}/\Delta A$ significantly different from values of models with similar fault geometries. Consequently, removing the results of models with high condition numbers does not greatly influence the overall distribution of $\Delta W_{ext}/\Delta A$, but only reduces the noise in this distribution.

The maximum $\Delta W_{ext}/\Delta A$ of the second stage of faulting (10.99 mJ/m^2) is only ~25% of the optimal gain in efficiency of the first stage (43.87 mJ/m^2), suggesting that fault propagation leads to successively smaller gains in efficiency throughout the development of the wedge. The maximum $\Delta W_{ext}/\Delta A$ of the second stage is likely lower than that of the first stage because slip

Figure 3
Results of work optimization search: change in external work divided by new fault area, ΔW_{ext} $/\Delta A$, for all tested geometries of first (A) and second (B) forethrust-backthrust pair thrusts. Sketches show range of fault geometries tested in work optimization search. Large ΔW_{ext} $/\Delta A$ indicates that added faults increase the efficiency of the system. Black circles indicate most efficient backthrust and forethrust geometries. Black contour lines show 10% increments of $\Delta W_{ext}/\Delta A$ relative to $\Delta W_{ext}/\Delta A$ of the most efficient backthrust or forethrust. $\Delta W_{ext}/\Delta A$ of optimal backthrust and forethrust in second stage are lower than $\Delta W_{ext}/\Delta A$ of optimal thrusts in first stage. The larger range of positions that produces >90% $\Delta W_{ext}/\Delta A$ of the optimal forethrust in second stage compared to the first stage suggests a reduced sensitivity of $\Delta W_{ext}/\Delta A$ to position in the second stage

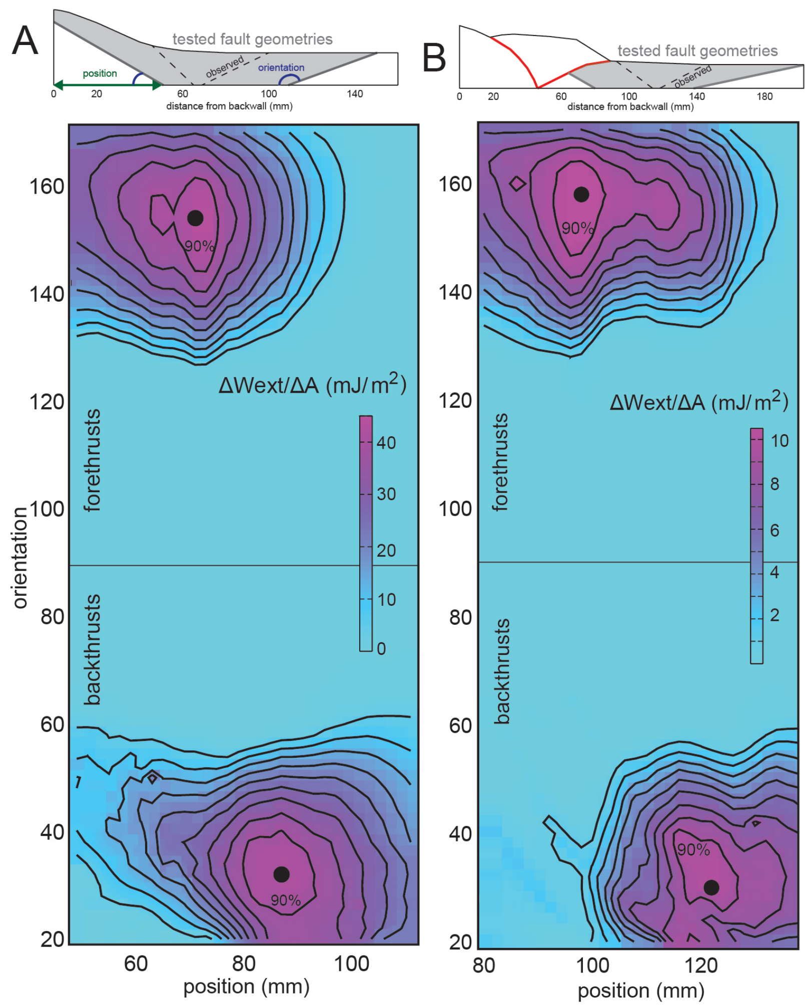

along pre-existing thrusts in the later stage contributes to efficiency of the system (W_{ext}) both before and after fault development.

4.2. Comparison of predicted and observed thrust geometry

In order to assess the predictions of work optimization, we compare the thrust geometry observed in the physical experiment to the most efficient thrust and the range of thrust geometries that have high efficiency (Fig. 4, Table 2). Because small scale material heterogeneities may cause faults to deviate from the precise prediction of the most efficient thrust geometry, we compare the observations to high-efficiency thrusts that produce >90% of the local maximum $\Delta W_{ext}/\Delta A$, and to moderately high-efficiency thrusts that produce >80% of the local maximum $\Delta W_{ext}/\Delta A$. The black contour lines overlaid on the full suite of numerical simulations (Fig. 3) are 10% intervals relative to each local maximum $\Delta W_{ext}/\Delta A$. Consequently, the extent of the high-efficiency and moderately high-efficiency thrusts may be extracted from Fig. 3. To directly compare the observed and the predicted thrust geometry, we overlay the extent of these efficient thrusts on the incremental shear strain field of the associated stages of the experiment (Fig. 4). For quantitative comparison of the observed and predicted fault geometries, we list the observed and predicted orientation and position of each thrust for each stage in Table 2.

For the first stage of faulting, the dip and location of the high-efficiency forethrusts (>90%) completely overlaps the observed forethrust, whereas the dip and location of the high-efficiency backthrusts only partly overlaps the geometry of the observed backthrust in the physical experiment (Fig. 4A-B, Table 2). The lower bound of the moderately high-efficiency (80%) backthrust positions differs from the observed position by more than 5 mm. The range of backthrusts that do overlap the observed position produce 60% of the local maximum $\Delta W_{ext}/\Delta A$. In the first stage of faulting, this work optimization analysis predicts the forethrust position, and backthrust and forethrust dips with success, but predicts the backthrust position less precisely.

The analysis of the second stage reveals that the dips of high-efficiency forethrusts and backthrusts (>90% of the maximum $\Delta W_{ext}/\Delta A$) both match the observed thrust dips (Fig. 4C-D, Table 2). Similarly, the positions of the high-efficiency thrusts closely match the observed positions (Fig. 4C-D, Table 2). The high-efficiency backthrusts that produce >90% of the

Table 2: Observed and predicted fault geometries

Stage	Thrust	Property	Observed	maximum $\Delta W_{ext}/\Delta A$	>90% max $\Delta W_{ext}/\Delta A$	>80% max $\Delta W_{ext}/\Delta A$
1	backthrust	position	65±7 mm	87 mm	81-93 mm	77-101 mm
		orientation	45±10°	32°	26-40°	20-42°
	forethrust	position	65±5 mm	71 mm	63-75 mm	57-77 mm
		orientation	156±4°	154°	146-160°	142-164°
2	backthrust	position	114±6 mm	122 mm	116-126 mm	114-134 mm
		orientation	38±5°	30°	20-40°	20-42°
	forethrust	position	114±5 mm	98 mm	94-102 mm	86-114 mm
		orientation	156±3°	158°	148-168°	144-168°

Observed and predicted positions and orientations of thrusts. Position is measured as the horizontal distance from the backwall to the root of the thrust. Orientation is measured clockwise from the left horizontal plane. We list the predicted range of the most efficient thrusts that produce the local maximum $\Delta W_{ext}/\Delta A$, the range of high-efficiency thrusts that produce >90% of the local maximum $\Delta W_{ext}/\Delta A$, and moderately high-efficiency thrusts that produce >80% of the local maximum $\Delta W_{ext}/\Delta A$ because small scale material heterogeneities may cause faults to deviate from the precise prediction of the most efficient thrust geometry. Except for the position of the backthrust in the first stage of faulting, the range of thrust orientations and positions that produce >80% of the local maximum $\Delta W_{ext}/\Delta A$ overlap the observed orientation and position.

maximum $\Delta W_{ext}/\Delta A$ completely overlap the observed backthrust, and the high-efficiency forethrusts overlap the upper two-thirds of the observed forethrust.

4.3. Influence of forethrust activity on backthrust development

The work optimization approach of this study closely predicts the geometry of many of the observed thrusts, with the weakest match to the backthrust position in the first stage of faulting (Fig. 4). In this stage, the basal location of the most efficient backthrust does not match the basal location of the most efficient forethrust, and so they do not form a commonly rooted forethrust-backthrust pair. This mismatch of the position of the most efficient thrusts suggests that the optimal geometry of thrusting may differ if our analysis searched for the optimal pair, rather than a single optimal thrust. Limit analysis predictions of the position and dips of the active forethrust-backthrust pair, rather than singular thrusts, have successfully matched the evolution of thrusting in accretionary systems [e.g., *Mary et al.,* 2013].

Observations of the physical experiment suggest that forethrust development may precede backthrust development. The incremental displacement and shear strain fields of the experiment reveal that shear strain localizes along a discrete forethrust-verging structure slightly before the backthrust fully forms (Fig. 1H). Furthermore, after the forethrust and backthrust both develop, the forethrust accommodates greater slip than the backthrust, suggesting that the forethrust acts as the dominant fault (Fig. 1I). The discrepancy between the positions of the predicted and observed backthrust may result from independently searching for the optimal backthrust geometry in a system that does not already include an active forethrust.

To determine how slip along the first forethrust may impact backthrust development, we search for the efficient geometry of the backthrust in a numerical wedge that represents the first stage of faulting immediately after the first forethrust develops. In this analysis, we compare $\Delta W_{ext}/\Delta A$ due to the development of backthrusts within the hanging wall of the forethrust, with dips from 30-90° and basal positions from 39-65 mm, in increments of 2° and 2 mm, respectively. The model boundary geometry, and material and fault properties are identical to those values used in the analysis of the first stage of faulting (Fig. 2, Table 1). However, whereas in the first analysis we use displacements observed in DIC increment 15, in this new analysis the loading conditions represent the increment of the experiment immediately after the first forethrust develops, DIC increment 16 (Fig. 5A-C).

Figure 5

A-C) Development of displacement loading conditions for numerical wedges that represent immediately after the first forethrust develops. Format and notation identical to Fig. 2. D) Results of work optimization search for geometry of first backthrust, after first forethrust forms. Format and notation identical to Fig. 3. E) Comparison of predicted and observed geometries of backthrust. Gray line shows pre-existing forethrust included in the model, otherwise the format is identical to Fig. 4. Fault geometries that produce >90% $\Delta W_{ext}/\Delta A$ of optimal backthrust completely overlap observed backthrust. These backthrusts share a common root with the pre-existing forethrust in the model.

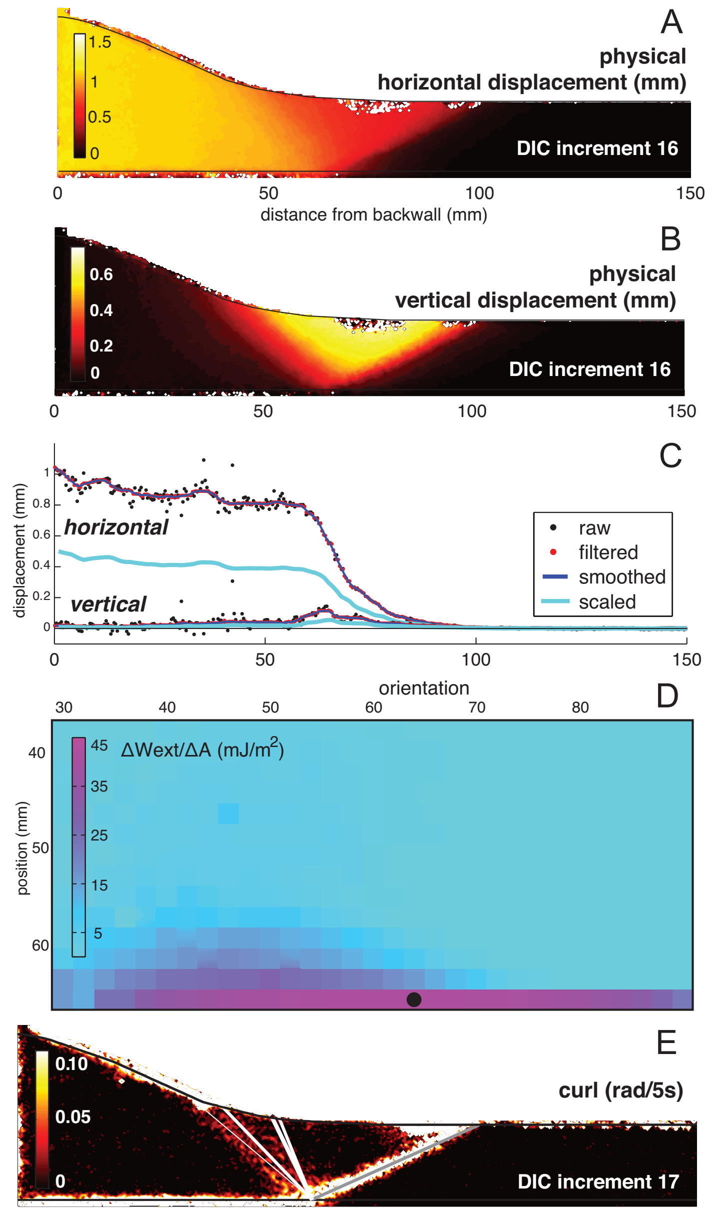

This analysis reveals that the optimal backthrust forms a pair with the pre-existing forethrust, and intersects the root of the forethrust (Fig. 5D-E). The range of backthrust geometries that produce >90% of the maximum $\Delta W_{ext}/\Delta A$ completely overlaps the region of high shear strain along the backthrust in the physical experiment. The improved prediction of the backthrust geometry in the system that includes the active forethrust suggests that deformation along the young forethrust promotes backthrust development, ultimately forming a backthrust-forethrust pair.

4.4. Comparison of Coulomb analysis and work optimization

To compare the orientations of planes that maximize Coulomb shear stress with the work optimization predictions, we calculate both the average and maximum Coulomb stress along faults of different orientations at the observed thrust root position in the first and second stages of faulting. This comparison reveals that the fault orientation that produces the maximum of the average Coulomb stress more closely matches the observed faulting than the orientation of the fault that hosts the maximum Coulomb stress (Fig. 6). In the first stage of faulting, the fault orientations that maximize the average Coulomb stress along the fault are within 2˚ of the orientation of faults with greatest efficiency (Fig. 6A-B). In the second stage of faulting, the fault orientations that maximize the average Coulomb stress along the fault differ by less than 4˚ from the orientations of the backthrust and forethrust that maximize $\Delta W_{ext}/\Delta A$ (Fig. 6E-F). These results suggest that the faults that accommodate deformation most efficiently are also those that have highest average Coulomb stress before slipping.

Next, we compare the orientations of planes that host the maximum Coulomb stress to the predictions of work optimization. When considering the onset of failure, we generally presume that the plane that hosts the maximum Coulomb stress is most likely to initiate and grow into a through-going fault. In the first stage of faulting, the orientations of the backthrust and forethrust that host the maximum Coulomb stress differ 12˚ and 6˚, respectively, from the most efficient, and differ 17˚ and 4˚, respectively, from the observed. In the second stage of faulting, the orientations of the backthrust and forethrust that host maximum Coulomb stress differ 12˚ and 10˚, respectively, from the most efficient, and differ 10˚ and 9˚, respectively, from the observed. The orientations of the fault planes with maximum Coulomb stress disagree with work optimization predictions and fall outside of the observed orientations for the backthrusts and

Figure 6
Comparison of work optimization and Coulomb predictions for first (A-D) and second (E-H) stages of faulting. Coulomb stress along planar faults at the observed location in the first (A) and second (E) stages of faulting. Orientation of planar faults vs. maximum and average Coulomb stress along faults in the first (B) and second (F) stages of faulting. Black vertical lines indicate observed orientations of backthrust and forethrust. Gray rectangles indicate extent of relatively high curl surrounding observed thrusts. Circles show maximum Coulomb stress of elements of planar fault at each orientation. Squares show average Coulomb stress of elements of planar fault at each orientation. Black circle and square indicates maximum of the maximum Coulomb stress and of the average Coulomb stress, respectively. C) Gain in efficiency, $\Delta W_{ext}/\Delta A$, produced by faults with various orientations at the position of the first observed backthrust-forethrust pair (65 mm). Black triangles indicate intersections of optimal faults with the model base and surface. Dashed lines show approximate geometry of observed thrusts. D) Orientation of faults at 65 mm from backwall vs. $\Delta W_{ext}/\Delta A$. G) Gain in efficiency, $\Delta W_{ext}/\Delta A$, produced by faults with various orientations at the observed position of the second backthrust-forethrust pair (114 mm). H) Orientation of faults at 114 mm from backwall vs. $\Delta W_{ext}/\Delta A$.

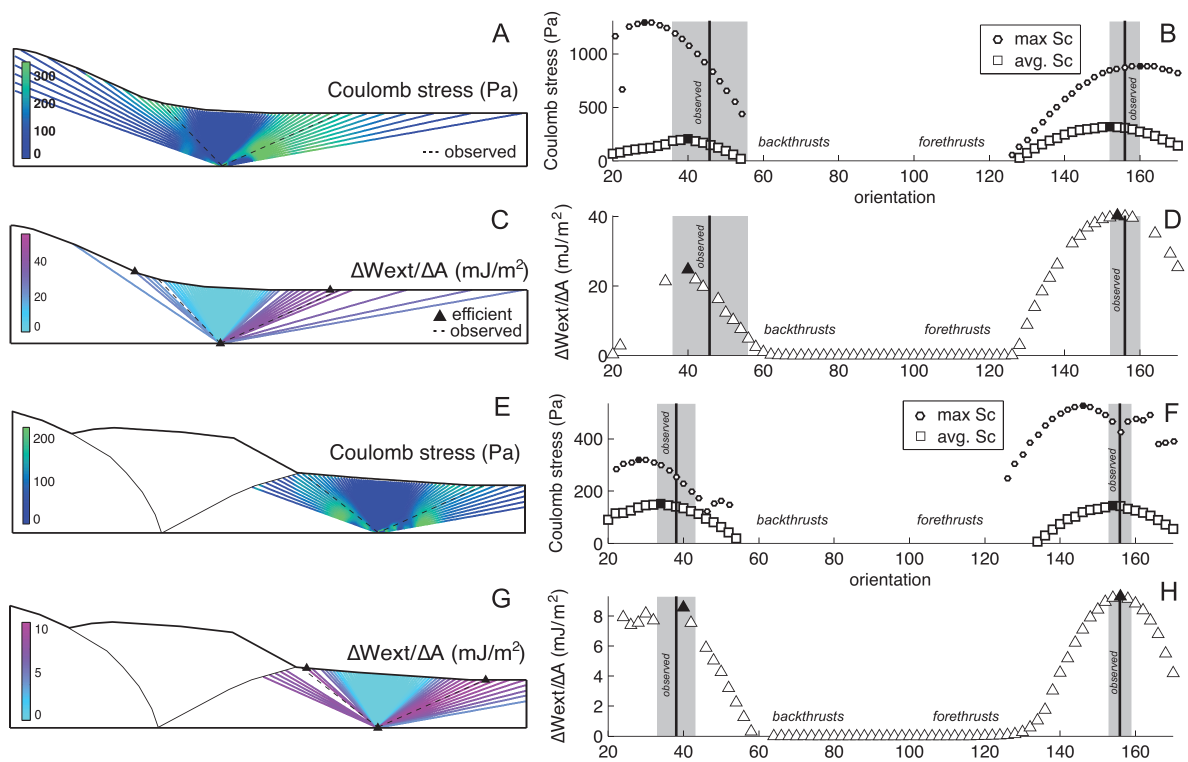

forethrusts at both stages of fault development. The closer agreement of the maximum average Coulomb stress and the efficient thrust geometry, compared to the maximum Coulomb stress approach, is consistent with the global approach of work optimization, which considers the stress state throughout the system. The average Coulomb stress considers the stress state along the length of the fault, rather than just the portion of the fault that hosts the maximum Coulomb stress.

In the first stage of faulting, the region of highest Coulomb stress, which indicates where incipient faults may initiate, differs between the backthrust and forethrust. For the backthrusts, highest Coulomb stress occurs near the top of the wedge and near the inflection of the wedge topography because local elastic flexure promotes shear along the thrusts (Fig. 6A). For the forethrusts, the highest Coulomb stress develops near the base of the wedge because the slip gradients along the detachment produce locally high shear stresses (Fig. 6A). In contrast, in the second stage of faulting, the highest Coulomb stress along both backthrusts and forethrusts arises near the wedge base because the wedge topography lacks an inflection outboard of the pre-existing thrusts at this stage (Fig. 6E).

4.5. Evolution of efficiency

To shed insight on the evolution of overall efficiency, we calculate the external work of wedge simulations with observed fault configurations at the first and second stages of faulting (Fig. 7). Each system tested differs from the other systems by the fault geometry and/or the applied displacement. The applied displacements of the earliest wedge simulations (systems 0-3) are derived from the displacements observed along the experiment base immediately before the development of the first thrust pair (DIC 15). The displacements of the next wedge simulation (system 4) uses the observed basal displacements immediately after the first thrust pair develops (DIC 16). To explore the second stage of faulting, the applied displacements of systems 5-8 simulate the basal displacements observed immediately before the second pair develops (DIC 47), and system 9 uses the basal displacements observed immediately after the second thrust pair develops (DIC 48). High external work (Eq. 1) indicates models with inefficient fault geometries that require large tractions along the model boundaries to accommodate the applied displacement.

Figure 7

A) Total slip along thrusts in numerical wedges at stages of wedge development. Fault geometry of numerical wedges represent the observed fault geometries. Systems 0-4 simulate the first stage of faulting, and use the displacements observed immediately before the first thrusts develop (systems 0-3, DIC increment 15, ~2 mm cumulative backwall displacement), and immediately after the first thrusts develop (system 4, DIC increment 16, ~3 mm cumulative backwall displacement). Systems 5-9 represent the second stage of faulting, immediately before thrusts in the second new pair develop (systems 5-8, DIC increment 47, ~38 mm cumulative backwall displacement), and immediately after the thrusts develop (system 9, DIC increment 48, ~39 mm cumulative backwall displacement). B) Evolution of efficiency, W_{ext}, for stages of wedge development. Fault development reduces W_{ext}, increasing overall efficiency. Fault development produces larger gains in efficiency (ΔW_{ext}) in the first stage compared to the second stage.

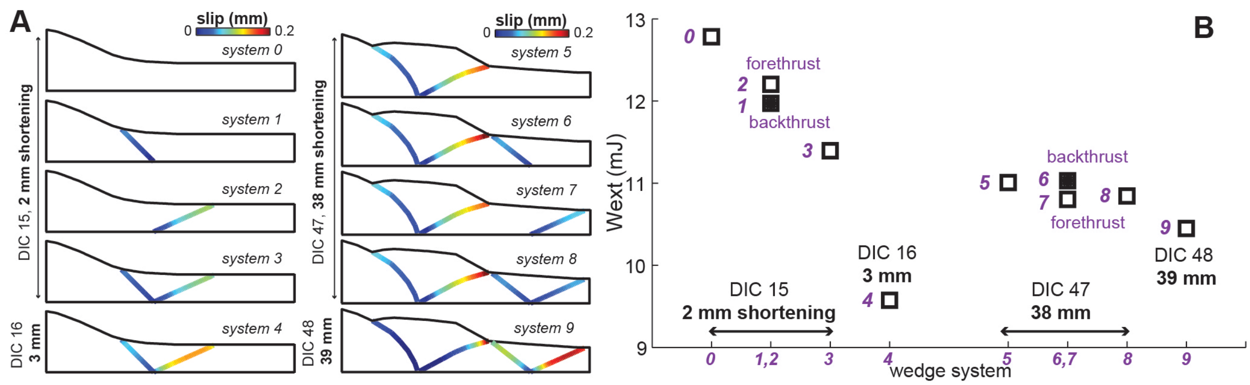

Before any faults develop in the wedge, the system is the least efficient and requires the greatest external work to accommodate the applied displacements (Fig. 7, system 0, W_{ext}=12.8 mJ). The development of the first backthrust-forethrust pair (system 3) increases the efficiency of the system to a greater extent than the backthrust (system 1) or forethrust (system 2) alone. The wedge requires the least external work to accommodate the applied displacements when the wedge includes the first thrust pair, and the applied boundary displacements simulate the incremental displacements immediately after that pair develops (system 4, 11.4 mJ). Because system 4 captures the retreat of the basal detachment fault tip to the root of the new thrust pair after they develop, system 4 more closely represents the deformation within the physical wedge containing the first thrust pair than system 3.

In the second stage of faulting, the additions of new faults produce smaller gains in efficiency than the first stage because the pre-existing thrusts continue to slip before and after new thrust development (Fig. 7). After the second backthrust-forethrust pair develops, and while the applied displacements simulate the detachment deformation observed preceding new fault development (system 8), the total slip summed along the thrusts of the second pair (102 mm) is only 28% of the slip along the pre-existing thrusts (363 mm). Updating the applied displacements to the detachment deformation observed just after the new thrust pair develops (system 9) increases the total summed slip along the second pair to 310 mm, and decreases the total slip along the pre-existing pair to 134 mm. Applying the displacements observed in the increment of the experiment immediately following the development of the second pair (system 9) captures the sharp decrease in detachment slip at the new thrust pair root, which promotes slip along the new backthrust and forethrust. Although greater slip along the new thrusts is associated with lesser slip along the pre-existing pair, the net effect reduces the total W_{ext} and increases system efficiency.

5. Discussion

The work optimization approach used in this study provides insight into two key stages of wedge development. The maximum gain in efficiency relative to new fault area, $\Delta W_{ext}/\Delta A$, produced by thrust development in the first stage is about four times higher than the maximum $\Delta W_{ext}/\Delta A$ of the second stage. This decrease in maximum $\Delta W_{ext}/\Delta A$ from the first to the second stage indicates that within accretionary wedges, the overall efficiency of the system becomes less sensitive to new fault development. In the following section 5.1, we compare the evolution of the numerical W_{ext} of simulations including the observed fault geometries to variations in physical normal force measured on the backwall in the experiment, which indicate changes in physical W_{ext}. Our results indicate that in the first stage of faulting, the backthrusts that produce the maximum $\Delta W_{ext}/\Delta A$ more closely match the observed backthrust geometry after the forethrust develops than before the forethrust develops. The agreement of the predicted and observed backthrust geometry following forethrust development suggests that the forethrust may propagate immediately before the backthrust, and thus control the position of the backthrust in the physical experiment. In the following discussion, we contrast the sensitivity of efficiency to forethrust position in the first and second stages of faulting. In the above analyses, we find that faults that maximize $\Delta W_{ext}/\Delta A$ more closely match the observed fault dip than planes that maximize Coulomb stress. However, the maximum average Coulomb stress along the entire fault predicts fault dips that closely match both the most efficient faults (max $\Delta W_{ext}/\Delta A$) and the observed faults. The distribution of Coulomb stress suggests that in the first stage of faulting, backthrusts may initiate near the top of the wedge, whereas forethrusts may initiate near the base, and in the second stage of faulting, both forethrusts and backthrusts are likely to initiate near the base. Below, we discuss factors that control the location of thrust initiation in physical, numerical, and crustal accretionary wedges. Tracking the evolution of W_{ext} throughout the first and second stages highlights that 1) thrust fault development increases the overall efficiency of the system, 2) updating the applied loading to match the observed distribution of detachment slip following thrust fault development increases slip on the modeled faults, and thus further increases system efficiency, and 3) thrust fault development and evolving boundary displacements produces larger gains in efficiency in the first stage than in the second stage of faulting. In the following discussion, we compare our numerical estimates of external work to physical measurements of external force on the accretion experiment.

5.1. Efficiency evolution of numerical and physical experiment

The evolution of efficiency in the numerical simulations is similar to the evolution of external normal force measured on the backwall throughout the physical experiment (Fig 8). The force increases upon the onset of loading and then decreases sharply with the growth of the first fault pair. The drop in backwall force with each episode of fault growth is consistent with other

Figure 8: Evolution of external work for stages of wedge development with force curve measured throughout physical accretion experiment E240. Consistent with the larger ΔW_{ext} produced by the development of the first pair relative to the second pair, the drop in force associated with the development of the first pair is larger than the drop associated with the second pair. Consistent with the increase in W_{ext} from system 4 to system 5, the force gradually rises following the development of the first pair to the second pair.

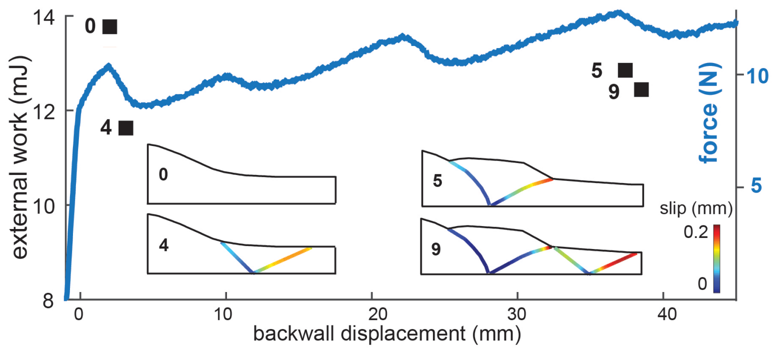

experimental results [*Cruz et al.*, 2010; *Cubas et al.*, 2010; *Souloumiac et al.*, 2012; *Herbert et al.*, 2015]. The numerical simulations also show decreases in external work associated with each episode of faulting. Between the episodes of new thrusting in physical experiments, the backwall force steadily increases [e.g., *Herbert et al.*, 2015]. In our numerical simulations, the external work on the numerical wedges increases from the conclusion of the first stage of faulting (system 4) to before the second pair forms (system 5) (Fig. 8). Through an analysis of the components of the work budget, *Del Castello & Cooke* [2007] show that thickening of the wedge between accretion episodes increases the frictional work on the detachment and underthrust, which subsequently increases the external work as the wedge deforms without faulting.

In addition to the overall increase in W_{ext} observed in the numerical simulations and inferred from the physical force measurements, fault development produces similar drops in the numerical W_{ext} and physical backwall force. The gain in efficiency (ΔW_{ext}) due to the development of the second pair (from system 5 to 9) is smaller than that gain due to the development of the first pair (from system 0 to 4) (Fig. 8). Consistent with this numerical result, the force measured on the backwall throughout the physical accretion experiment reveals a greater drop associated with the development of the first pair, than the second (Fig. 8). Within the numerical simulation, the development of the second thrust pair produces smaller ΔW_{ext} than the first pair because the pre-existing thrust pair continues to slip after the development of the new thrusts. Consequently, the addition of the new pair has less impact on the overall fault network. In particular, the persistent slip along the pre-existing forethrust causes the nearby region of high strain energy density (SED), indicative of off fault deformation and internal mechanical work [e.g., *Jaeger et al.*, 2007], to remain after the new pair develops (Fig. S3).

5.2. Sensitivity of efficiency to forethrust position

Differences between the range of highly efficient forethrust positions in the first and second stage suggests that $\Delta W_{ext}/\Delta A$ is more sensitive to position in the first stage of fault development than the second stage. In particular, the range of forethrust positions that produce >80% of the maximum forethrust $\Delta W_{ext}/\Delta A$ in the second stage (30 mm) is wider than that range in the first stage of faulting (20 mm). The varying sensitivity of efficiency to forethrust position arises from differences in the gradient of the basal displacements in the first and second stages of thrust faulting. High gradients in the basal displacement produce localized regions of high SED within the wedge (Fig. 9). Fault tips and other irregularities typically produce regions of high SED, and numerical analyses indicate that fractures tend to propagate into regions of high SED [e.g., *Du and Aydin*, 1993, 1996; *Olson and Cooke*, 2005; *Okubo and Schultz,* 2005]. SED is the product of stress and strain and measures the internal mechanical work [e.g., *Jaeger et al*., 2007].

Prior to the first stage of thrust faulting, the applied basal displacements produce a localized region of high SED from ~70-90 mm from the backwall (Fig. 9A). In contrast, prior to the second stage, the applied displacements produce a wider region of high SED from ~90-130 mm from the backwall (Fig. 9B). The smaller region of high SED in the first stage results from the sharper gradient in the applied horizontal basal displacements, compared to the second stage of faulting (Fig. 9C). In the first stage of faulting, the sharp displacement gradient and associated high SED region occur in the region where the most efficient forethrusts form, suggesting that this localization of internal strain controls the predicted position of the thrusts. In contrast, in the second stage of faulting, the gentler displacement gradient results in a wider region of high SED, and a corresponding reduced sensitivity of $\Delta W_{ext}/\Delta A$ to horizontal position.

These gradients in the applied displacements arise from slip gradients along the basal detachment fault within the physical experiment. In the first stage of faulting, the distribution of slip along the physical wedge base produced by the detachment fault has a sharp decrease in slip near the location of incipient faulting. In contrast, during the second stage of faulting, the detachment produces a more gradual slip gradient so that the position of thrust faulting is not as strongly controlled by the slip gradient as it is for the first stage of faulting. Applying the effects of this slip gradient to the base of our models provides a method of incorporating the local concentration of SED arising from the slip gradient along the detachment.

The correlation of the sensitivity of $\Delta W_{ext}/\Delta A$ to forethrust position and extent of high SED suggests that off-fault deformation may control the position of new faults. The work stored in off-fault deformation, which is the internal work of the system, is calculated as the integrated SED field [e.g., *Cooke & Madden*, 2014]. Consequently, the growth and shrinkage of high SED regions indicate increasing and decreasing internal work. The spatial correlation between locations of thrust development and areas of high SED regions further supports the inference that off-fault deformation controls new thrust position. In addition, the spatial correlation of the predicted highly efficient forethrusts with observed forethrusts in both stages of faulting indicates that forethrusts develop within high SED regions. Such fault growth decreases off-fault

Figure 9: Strain energy density (SED) produced in numerical wedges representing first (A) and second (B) stage of faulting. White lines indicate geometries of most efficient forethrust (thickest line), forethrusts that produce >90% of maximum forethrust $\Delta W_{ext}/\Delta A$ (thinner lines), and forethrusts that produce >80% of maximum forethrust $\Delta W_{ext}/\Delta A$. C) Horizontal and vertical displacements applied to base of numerical wedges. The region of high SED is more localized in first stage than region in second stage. The range of predicted positions of efficient forethrust geometries is smaller in first stage. The gradient in applied horizontal displacements is larger in first stage than in second stage near the position where the observed thrusts develop.

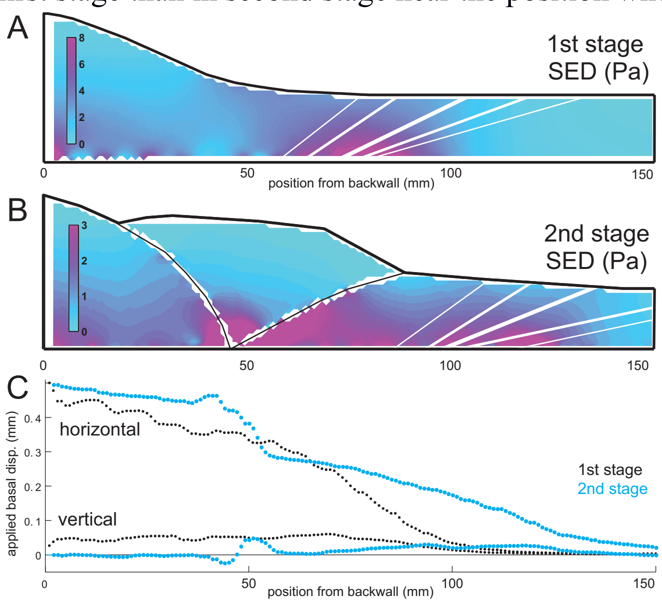

deformation and increases the overall efficiency within both the numerical simulations and physical experiments.

5.3. Comparison of numerical and physical estimates for W_{prop}

We observe first-order similarities between the evolution of the numerical W_{ext} and physical backwall force (section 5.1), and links between the internal work (SED) and the observed physical forethrust position (section 5.2). To assess differences in energy partitioning in the physical and numerical wedges, we compare the numerical and physical estimates of the changes in W_{ext} due to fault growth. The increase of W_{ext} between episodes of new fault development reveals that energy must accumulate within the fault system before it reaches the value required for the creation of new fault surfaces [*Del Castello & Cooke*, 2007]. Consequently, the energy required to create new fault surfaces, $W_{prop,}$ can be determined from the change in W_{ext} and forces on the system preceding and following fault development [*Herbert et al.,* 2015]. *Herbert et al.* [2015] calculate W_{prop} for the same physical accretion experiment simulated here (E240) from the change in force measured on the backwall and the distance over which the force drop occurs. In a sandpack of 16 mm thickness, W_{prop} is 104±60 mJ/m^2 [*Herbert et al*., 2015]. To compare our numerical results to the physical estimates of $W_{prop,}$ we scale our model displacement (0.5 mm) to the total displacement over which the faults develop (2 mm), and assume that W_{ext} scales linearly for the development of the first forethrust-backthrust pair. Incremental loading of the numerical wedge that contains the observed geometry of the backthrust and forethrust in the first stage of faulting (Fig. 7, system 3) reveals that W_{ext} increases approximately linearly after the loading increment in which slip occurs along the complete lengths of both faults (R^2=0.989, Fig. S4). Although frictional slip is inelastic and may account for the deviance from purely linear, its small influence in these models suggests that W_{ext} may be linearly approximated.

Our scaled numerical estimates yield similar magnitudes to the $W_{prop}/\Delta A$ estimated from external force for the experiment simulated here (104±60 mJ/m^2) [*Herbert et al*., 2015]. In the numerical simulations of this experiment, the $\Delta W_{ext}/\Delta A$ due to the development of the first forethrust-backthrust pair is approximately 20 mJ/m^2 for 0.5 mm of moving wall displacement. For the observed displacement range (1.90 to 2.41 mm), the derived values of $\Delta W_{ext}/\Delta A$ scale as 76.1 to 96.4 mJ/m^2, a close match to the experimentally determined value.

To compare our estimates of the energy consumed in fault growth in dry sand to crustal estimates of the energy to create crustal faults over several thousand earthquakes, we upscale W_{prop}. Our estimates of W_{prop} incorporate the work consumed for the thrust faults to grow to their through-going length. Whereas the thrust faults develop by creep in the experiment, crustal faults reach maturity over many (i.e., 10^2-10^3) earthquakes. Consequently, we upscale our estimates of W_{prop} (10^{-1} J/m^2) to crustal length scales by multiplying by the scaling ratio (10^5:1) [e.g., *Hubbert*, 1937]. The resulting crustal scale estimate (10^4 J/m^2) multiplied by the approximate number of slip events that produce mature faults yields 10^6-10^7 J/m^2. This *upscaled laboratory estimate* is comparable to the 10^5-10^6 J/m^2 estimates of work of fault growth from field observations of comminution within fault zones [e.g., *Chester et al.*, 2005; *Wilson et al.*, 2005; *Pittarello et al.*, 2008; *Xie & Kato*, 2017]. In addition, the consistency of the W_{prop} estimates, as well as the agreement between the predicted and observed thrust geometry, and the numerical and physical fault slip distribution, indicates that these numerical accretion simulations closely represent deformation of the physical wedge.

5.4. Thrust fault initiation location and orientation within accretionary wedges

High temporal resolution monitoring of physical accretion experiments reveals formation of a zone of short-lived shear bands prior to localization of a single thrust [*Bernard et al.*, 2007; *Dotare et al.*, 2016]. These transient shear bands tend to have uniform slip; however, some bands accommodate greater slip near the wedge base [*Bernard et al.*, 2007; *Dotare et al.*, 2016], while others only slip near the top of the sandpack [*Dotare et al.*, 2016]. These differing patterns of shear strain suggest that incipient thrusts may initiate at a variety of depths within physical wedges. Interpretations of seismic images of the protothrust regions of crustal accretionary wedges indicate that thrusts may initiate above the detachment and propagate both upwards and downwards [e.g., *Morgan & Karig,* 1995].

In the numerical wedges analyzed here, local elevated Coulomb stresses develop at a variety of depths (Fig. 6). Gradients in basal detachment slip, which we simulate with basal displacements, produce local zones of high shear stress near the base of the model that increase Coulomb stress on the down-dip portions of shallower dipping forethrusts in the first stage (Fig. 6A), and both verging thrusts in the second stage of faulting simulated (Fig. 6E). Consequently, if the physical accretionary wedges are sufficiently homogeneous and isotropic so that pre-existing weaknesses do not control thrust fault growth, we might expect the initiation of thrust faults near the base of the experiment. However, in the numerical simulations of the first stage of thrust development, the uplift of the left portion of the model relative to the right portion produces local elastic flexure near the inflection of the wedge topography, which increases the local shear stresses. These shear stresses promote elevated Coulomb stress on the updip portions of backthrusts that approach the surface (Fig. 6A). However, in physical wedges, sand grain movement is not purely elastic as in these numerical wedge simulations. Consequently, the local flexure near the modeled surface inflection may concentrate shear stresses to a greater degree in the simulations than in physical sand experiments where stress concentrations can dissipate through diffuse grain rearrangement.

Within crustal wedges, many processes may concentrate shear stresses and promote thrust initiation near the detachment. For example, non-planar subducting oceanic crust topography may locally concentrate stresses [e.g., *Park et al*., 1999; *Dominguez et al*., 2000]. Furthermore, fluid expulsion from dewatering sediments [e.g., *Bray & Karig*, 1985] may provide heterogeneous strength that would promote failure in some regions over others, or nucleate fractures that ultimately coalesce into faults. Strength variations within wedge units, such as lithologic variations and pre-existing weaknesses may promote thrust initiation above the detachment. Within the interseismic period in crustal wedges, slip gradients may develop along the detachment near the updip limit of the seismogenic zone, where slip behavior transitions from velocity weakening (locked) to velocity strengthening (aseismic slip) [e.g., *Wang & Hu*, 2006]. However, these gradients do not persist over the many earthquake cycles considered in the physical accretion experiment, and in the numerical simulations of this experiment.

The difference between the dip of planes with maximum local Coulomb stress and dip of planes with largest average Coulomb stress may provide insight into the process of thrust initiation. Our analyses indicate that the orientation of planes that host the maximum Coulomb stress differs from the experimentally observed fault dips, whereas the orientation of faults the host the largest Coulomb stress averaged along the fault more closely match the observed fault dips. The mismatch suggests that while faults may initiate within regions of highest Coulomb stress, the overall development of the fault may follow the surface that has greatest average Coulomb stress, which also produces large gains in overall efficiency (Fig. 6). In experiments of strike-slip fault initiation, the orientation of active shear planes changes from the initiation of *en* *echelon* shears to the development of a through-going fault [e.g., *Tchalenko*, 1970]. Similar coalescence processes may occur throughout the development of thrust faults within accretionary systems.

6. Conclusions

The work optimization framework provides a computationally inexpensive method to predict fault development. Within simulations of two stages of a physical sandbox accretion experiment, the planar through-going fault configurations that produce the largest changes in external work per new fault area, $\Delta W_{ext}/\Delta A$, closely match the observed geometries of new forethrust-backthrust pairs. The agreement of the predicted efficient geometries and the observed geometries provide additional support to the concept that tectonic systems evolve in order to minimize the total work of the system. At the position of the observed thrusts, the dips of the most efficient backthrust and forethrust match within 4º of the observed dips, and consistently more closely match the observed orientation than the planes with maximum Coulomb stress. However, fault planes that maximize the average Coulomb stress along the faults at the position of the observed thrusts more closely match the dip of the most efficient thrusts and the observed thrusts. This result suggests that using the average Coulomb stress along through-going faults, as well as the gain in efficiency due to thrust development, produce more successful predictions of thrust fault dip than assessing the maximum Coulomb stress at points of potential fault initiation. The match of the backthrust prediction in simulations that include a pre-existing forethrust, and the strain evolution of the physical experiment revealed with digital image correlation (Fig. 1), suggest that forethrust development precedes backthrust growth in the first stage of faulting. In contrast to traditional approaches of predicting fault development in accretionary wedges, in which the wedge does not include pre-existing weaknesses, our conclusion that forethrust slip influences backthrust development indicates that considering the effects of pre-existing fault slip within the wedge will improve predictions of fault evolution in accretionary wedges. The elevated $\Delta W_{ext}/\Delta A$ due to the propagation of the first backthrust-forethrust pair, as compared to the second pair, indicates that if pre-existing thrusts continue to slip, the propagation of new thrusts may lead to increasingly smaller gains in efficiency as the accretionary wedge evolves. The diminishing gains in efficiency due to fault growth suggests that in mature crustal wedges, fault development may only minimally perturb overall wedge efficiency if pre-existing wedge faults continue to slip. If pre-existing faults shut off prior to new fault development, then increasing strain will be stored within the host material prior to new fault growth, and new fault development may produce significant gains in efficiency. The similar estimates of experimental $W_{prop}/\Delta A$ and numerical $\Delta W_{ext}/\Delta A$, and similar evolution of experimental force drops and numerical ΔW_{ext} due to fault development suggest that analysis of the evolving efficiency may be exacted with confidence in both numerical and physical experiments. In this contribution, integrating quantitative observations of physical accretion experiments and analyses of numerical simulations enabled the comparison of predictions of work minimization and Coulomb stress with the observed, physical faults. Using work optimization to assess the order of thrust development may provide additional insight into the mechanics of frontal accretion thrust vergence, which could indicate the likelihood of shallow megathrust rupture [*Cubas et al.*, 2016].

8. Acknowledgements

The data from the laboratory experiment have been uploaded to the repository for physical models run by GFZ Data Services [*Souloumiac et al*., 2017]. The numerical modelling software (Fric2D) is available from GitHub as part of the GROW package of tools (https://github.com/mlcooke/GROW). The numerical models are available on request. This work was supported in part by two Geological Society of America student research grants to JM, and an International Association of Mathematical Geologists Computers & Geosciences student research grant to JM, as well as National Science Foundation grant EAR-1019747 to MC. The insightful comments of an anonymous reviewer, reviewer Dr. Morgan and the associate editor Dr. Kaneko helped improve this manuscript.

References

Abercrombie, R. E., & J. R. Rice (2005). Can observations of earthquake scaling constrain slip weakening?. *Geophysical Journal International*, *162*(2), 406-424.

Adam, J., D. Klaeschen, N. Kukowski, and E. Flueh (2004), Upward delamination of Cascadia Basin sediment infill with landward frontal accretion thrusting caused by rapid glacial age material flux, *Tectonics*, *23(3)*, 1-21.

Adam, J., and C. D. Reuther (2000), Crustal dynamics and active fault mechanics during subduction erosion: Application of frictional wedge analysis on to the North Chilean Forearc, *Tectonophysics*, 321, 297–325.

Adam, J., J. L. Urai, B. Wieneke, O. Oncken, K. Pfeiffer, N. Kukowski, J. Lohrmann, S. Hoth, W. van der Zee, and J. Schmatz (2005), Shear localisation and strain distribution during tectonic faulting—new insights from granular-flow experiments and high-resolution optical image correlation techniques, *J. Struct. Geol*., *27*, 283–301, doi:10.1016/j.jsg.2004.08.008.

Baba, T., T. Hori, S. Hirano, P.R. Cummins, J.O. Park, M. Kameyama, and Y. Kaneda (2001), Deformation of a seamount subducting beneath an accretionary prism: constraints from numerical simulation, *J. Geophys. Res*., *28(9)*, 1827-1830.

Bangs, N.L., T.H. Shipley, S.P. Gulick, G.F. Moore, S. Kuromoto, and Y. Nakamura (2004), Evolution of the Nankai Trough décollement from the trench into the seismogenic zone: Inferences from three-dimensional seismic reflection imaging, *Geology*, *32(4)*, 273-276.

Barnes, P.M., B. Davy, R. Sutherland, and J. Delteil (2002), Frontal accretion and thrust wedge evolution under very oblique plate convergence: Fiordland Basin, New Zealand, *Basin Res*., *14(4)*, 439-466.

Bernard, S., J.-P. Avouac, S. Dominguez, and M. Simoes (2007), Kinematics of fault-related folding derived from a sandbox experiment, *J. Geophys. Res., 112,* B03S12, doi: 10.1029/2005JB004149.

Bigi, S., L. Di Paolo, L. Vadacca, and G. Gambardella (2010), Load and unload as interference factors on cyclical behavior and kinematics of Coulomb wedges: insights from sandbox experiments, *J. Struct. Geol*., *32(1)*, 28-44.

Buiter, S.J. (2012), A review of brittle compressional wedge models, *Tectonophysics*, *530*, 1-17.

Bray, C. J., & D. Karig, (1985). Porosity of sediments in accretionary prisms and some implications for dewatering processes. *Journal of Geophysical Research: Solid Earth*, *90*(B1), 768-778.

Burbidge, D.R., and J. Braun, (2002), Numerical models of the evolution of accretionary wedges and fold-and-thrust belts using the distinct-element method, *Geophys. J. Int*., *148*, 542-

561.

Byrne, T. and D. Fisher (1987), Episodic growth of the Kodiak convergent margin, *Nature*, *325*, 338-341.

Chester, J.S., F.M. Chester, and A.K. Kronenberg (2005), Fracture surface energy of the Punchbowl fault, San Andreas system. *Nature*, *437(7055)*, 133-136.

Cooke, M.L., and E. H. Madden (2014), Is the Earth lazy? A review of work minimization in fault evolution, *J. Struct. Geol*., *66*, 334–346, doi:10.1016/j.jsg. 2014.05.004.

Cooke, M.L., and S. Murphy (2004), Assessing the work budget and efficiency of fault systems using mechanical models. *J. Geophys. Res: Solid Earth*, *109*(B10).

Cooke, M.L., and D. D. Pollard (1997), Bedding plane slip in initial stages of fault-related folding, *J. Struct. Geol*., *19*, 567-581.

Cruz, L., J. Malinski, A. Wilson, W.A. Take, and G. Hilley (2010), Erosional control of the kinematics and geometry of fold-and-thrust belts imaged in a physical and numerical sandbox, *J. Geophys. Res: Solid Earth*, *115*(B9).

Cubas, N., Y.M. Leroy, and B. Maillot (2008), Prediction of thrusting sequences in accretionary wedges, *J. Geophys. Res*., *113*, B12412, doi:10.1029/2008JB005717.

Cubas, N., B. Maillot, and C. Barnes (2010), Statistical analysis of an experimental compressional sand wedge, *J. Struct. Geo.*, *32*, 818-831, doi:10.1016/j.jsg.2010.05.010.

Cubas, N., C. Barnes, and B. Maillot (2013), Inverse method applied to a sand wedge: estimation of friction parameters and uncertainty analysis, *J. Struct. Geo.*, *55*, 101-113.

Cubas, N., P. Souloumiac, and S. Singh (2016), Relationship link between landward vergence in accretionary prisms and tsunami generation, *Geology*, doi:10.1130/G38019.1

Dahlen, F. (1984), Noncohesive critical Coulomb wedges: An exact solution, *J. Geophys. Res*., *89*, 10125-10133.

Dahlen, F. A. (1990), Critical taper model of fold-and-thrust belts and accretionary wedges, *Annu. Rev. Earth Planet. Sci*., *18*, 55–99.

Dahlen, F.A., J. Suppe and D. Davis (1984), Mechanics of fold-and-thrust belts and accretionary wedges: cohesive coulomb theory, *J. Geophys. Res.*, *89*(B12), 10087–10101.

Davey, F.J., M. Hampton, J. Childs, M.A. Fisher, K. Lewis, and J.R. Pettinga (1986), Structure of a growing accretionary prism, Hikurangi margin, New Zealand, *Geology*, *14(8*), 663-666.

Davis, D., J. Suppe and F. Dahlen (1983), Mechanics of fold-and-thrust belts and accretionary wedges, *J. Geophys. Res*., *88*, 1153-1172.

Del Castello, M., and M.L. Cooke (2007), Underthrusting-accretion cycle: work budget as revealed by the boundary element method, *J. Geophys. Res*., *113*, B12404, 1–14, doi:10.1029/2007JB004997.

Dominguez, S., J. Malavieille, & S. Lallemand (2000), Deformation of accretionary wedges in response to seamount subduction: Insights from sandbox experiments. *Tectonics*, *19*(1), 182-196.

Dotare, T., Y. Yamada, J. Adam, T. Hori and H. Sakaguchi (2016), Initiation of a thrust fault revealed by analog experiments, *Tectonophysics*, doi: 10.1016/j.tecto.2015.12.023.

Du, Y. and A. Aydin (1993), The maximum distortional strain energy density criterion for shear fracture propagation with applications to the growth paths of en echelon faults, *Geophys. Res. Lett.*, *20*(11), 1091-1094.

Du, Y. and A. Aydin (1996), Is the San Andreas big bend responsible for the Landers earthquake and the eastern California shear zone?, *Geology*, *24*(3), 219-222.

Ellis, S., C. Beaumont and O. A. Pfiffner (1999), Geodynamic models of crustal-scale episodic tectonic accretion and underplating in subduction zones, *J. Geophys. Res.: Solid Earth, 104(B7)*, 15169-15190.

Ellis, S., G. Schreurs, and M. Panien (2004), Comparisons between analogue and numerical models of thrust wedge development, *J. Struct. Geo., 26(9)*, 1659-1675.

Graveleau, F., J. Malavielle, and S. Dominquez (2012), Experimental modelling of orogenic wedges: a review, *Tectonophysics, 538–540*, 1–66, doi:10.1016/j.tecto.2012.01.027.

Gulick, S.P.S., N.L.B. Bangs, T.H. Shipley, Y. Nakamura, G. Moore, and S. Kuramoto (2004), Three-dimensional architecture of the Nankai accretionary prism's imbricate thrust zone off Cape Muroto, Japan: Prism reconstruction via en echelon thrust propagation, *J. Geophys. Res.: Solid Earth, 109*(B2), 2156-2202, doi:10.1029/2003JB002654.

Gutscher, M., N. Kukowski, J. Malavieille, and S. Lallemand (1996), Cyclical Behavior in Thrust Wedges: Insights from High Basal Friction Sandbox Experiments, *Geology, 24*, 135-138.

Gutscher, M.A., N. Kukowski, J. Malavieille, and S. Lallemand (1998), Episodic imbricate thrusting and underthrusting: analog experiments and mechanical analysis applied to the Alaskan Accretionary Wedge, *J. Geophys. Res., 103*, 10,161-10,176.

Haq, S.S. (2012), Out-of-sequence thrusting in experimental Coulomb wedges: Implications for the structural development of mega-splay faults and forearc basins, *Geophys. Res. Lett., 39(20)*, L20306, 1-5.

Hardy, S., C. Duncan, J. Masek, and D. Brown (1998), Minimum work, fault activity and the growth of critical wedges in fold and thrust belts, *Basin Res., 10*, 365–373., doi:/10.1046/j.1365-2117.1998.00073.x.

Herbert, J.W. (2014), Investigating fault system deformation with numerical models and analog experiments, Ph. D. thesis, Dep. of Geosciences, Univ. of Massachusetts, Amherst, Massachusetts, USA.

Herbert, J.W., M.L. Cooke, P. Souloumiac, E.H. Madden, B.C. Mary and B. Maillot (2015), The work of fault growth in laboratory sandbox experiments, *Earth Planet. Sci. Lett., 432*, 95-102.

Hoth, S. (2005), Deformation, erosion, and natural resources in continental collision zones – insight from scaled sandbox simulations, PhD thesis. Geo-Forschungs Zentrum Potsdam, Potsdam, Germany. 141.

Hubbert, M. K. (1937), Theory of scale models as applied to the study of geologic structures, *Bull. Geol. Soc. Am.*, 48(10), 1459–1519.

Huiqi, L., K.R. McClay, and D. Powell (1992), Physical models of thrust wedges. In *Thrust Tectonics*, edited by K. R. McClay, Chapman and Hall, London, 71-8l, doi: 10.1007/978-94-011-3066-0.

Jaeger, J. C., N.G. Cook, and R.W. Zimmerman, (2007), Fundamentals of Rock Mechanics, Blackwell Publishing.

Knupp, P. M., (2000). Achieving finite element mesh quality via optimization of the Jacobian matrix norm and associated quantities. Part II—a framework for volume mesh optimization and the condition number of the Jacobian matrix, *International Journal for numerical methods in engineering*, *48*(8), 1165-1185.

Konstantinovskaia, E., and J. Malavieille, (2005), Erosion and exhumation in accretionary orogens: experimental and geological approaches, *Geochem. Geophys. Geosyst., 6* (*Q02006*), doi: 10.1029/2004GC000794.

Konstantinovskaya, E., and J. Malavieille, (2011), Thrust wedges with décollement levels and syntectonic erosion: a view from analogue models, *Tectonophysics, 502 (3–4*), 336–350.

Kopp, C., J. Fruehn, E.R. Flueh, C. Reichert, N. Kukowski, J. Bialas, and D. Klaeschen (2000), Structure of the Makran subduction zone from wide-angle and reflection seismic data, *Tectonophysics, 329(1*), 171-191.

Kopp, H., and N. Kukowski (2003), Backstop geometry and accretionary mechanics of the Sunda margin, *Tectonics, 22(6*), 1072, doi:10.1029/2002TC001420.

Koyi, H.A., and J. Cotton (2004), Experimental insights on the geometry and kinematics of fold-and-thrust belts above weak, viscous evaporitic décollement; a discussion, *J. Struct. Geo., 26(11)*, 2139–2141.

Krantz, R.W. (1991), Measurements of friction coefficients and cohesion for faulting and fault reactivation in laboratory models using sand and sand mixtures, *Tectonophysics, 188 (1–2*), 203–207, doi:10.1016/0040-1951[91]90323-K.

Lallemand, S., P. Schnrle, and J. Malavieille (1994), Coulomb theory applied to accretionary and nonaccretionary wedges: Possible causes for tectonic erosion and/or frontal accretion, *J. Geophys. Res., 99*, 12033-12055.

Lambe, T.W., and R.V. Whitman (1969), Soil Mechanics, 553, John Wiley Press, New York.

Lohrmann, J., N. Kukowski, J. Adam, and O. Oncken (2003), The impact of analogue material properties on the geometry, kinematics, and dynamics of convergent sand wedges, *J. Struct. Geol., 25*, 1691–1711, doi:/10.1016/S0191- 8141[03]00005-1.

Maillot, B. (2013), A sedimentation device to produce uniform sand packs, *Tectonophysics, 593*, 85–94, doi:/10.1016/j.tecto.2013.02.028.

Maillot, B., C. Barnes, J.M. Mengus, and J.M. Daniel (2007), Constraints on friction coefficients by an inverse analysis of sand box thrust dips, *J. Struct. Geol., 29*, 117– 128.

Maillot, B., and H. Koyi (2006), Thrust dip and thrust refraction in fault-bend folds: Analogue models and theoretical predictions, *J. Struct. Geol., 28*, 36– 49.

Maillot, B., and Y.M. Leroy (2003), Optimal dip based on dissipation of back thrusts and hinges in fold-and-thrust belts, *J. Geophys. Res.*, *108*(B6).

Malavielle, J. (2010), Impact of erosion, sedimentation, and structural heritage on the structure and kinematics of orogenic wedges: analog models and case studies, *GSA Today, 20(1*), 4–10.

Mary, B.C.L., B. Maillot, and Y.M. Leroy (2013), Deterministic Chaos in frictional wedges revealed by convergence analysis, *Int. J. Num. Anal. Methods Geomech., 37*, 3036–3051, http://dx.doi.org/10.1002/nag.2177.

McBeck, J., E. Madden, and M. L. Cooke (2016), Growth by Optimization of Work (GROW): A new modeling tool that predicts fault growth through work minimization, *Comput. Geosci., 88*, 142-151.

McClay, K. R., and P.S. Whitehouse (2004), Analog modeling of doubly vergent thrust wedges, in *Thrust Tectonics and Hydrocarbon Systems*, edited by K. R. McClay, AAPG Mem., 82, 187 – 209.

Miyakawa, A., Y. Yamada, and T. Matsuoka (2010), Effect of increased shear stress along a plate boundary fault on the formation of an out-of-sequence thrust and a break in surface slope within an accretionary wedge, based on numerical simulations, *Tectonophysics, 484(1)*, 127-138.

Moore, G.F., T.H. Shipley, P.L. Stoffa, D.E. Karig, A. Taira, S. Kuramoto, H. Tokuyama and K. Suyehiro (1990), Structure of the Nankai Trough accretionary zone from multichannel seismic reflection data, *J. Geophys. Res.: Solid Earth, 95(B6*), 8753-8765.

Moore, J.C., J. Diebold, M.A. Fisher, J. Sample, T. Brocher, M. Talwani, J. Ewing, R. von Huene, C. Rowe, D. Stone, and C. Stevens (1991), EDGE deep seismic reflection transect of the eastern Aleutian arc-trench layered lower crust reveals underplating and continental growth, *Geology, 19(5*), 420-424.

Moore, G.F., D. Saffer, M. Studer, and P. Costa Pisani (2011), Structural restoration of thrusts at the toe of the Nankai Trough accretionary prism off Shikoku Island, Japan: Implications for dewatering processes, *Geochem. Geophys. Geosyst., 12(5*), Q0AD12, doi: 10.1029/2010GC003453.

Morgan, J.K. and D.E. Karig (1995), Kinematics and a balanced and restored cross-section across the toe of the eastern Nankai accretionary prism, *J. Struct. Geo., 17(1*), 31-45.

Mulugeta, G. (1988), Modelling the geometry of Coulomb thrust wedges, *J. Struct. Geo., 10*, 847–859.

Mulugeta, G., and H. Koyi (1992), Episodic accretion and strain partitioning in a model sand wedge, *Tectonophysics, 202(2*), 319-333.

Naylor, M., H.D. Sinclair, S. Willett, and P.A. Cowie (2005), A discrete element model for orogenesis and accretionary wedge growth*, J. Geophys. Res.: Solid Earth, 110*(B12).

Nemcok, M., M.P. Coward, W.J. Sercombe and R.A. Klecker (1999), Structure of the West Carpathian accretionary wedge: insights from cross section construction and sandbox validation*, Physics and Chemistry of the Earth, Part A: Solid Earth and Geodesy, 24(8*), 659-665.

Okubo, C.H., and R.A. Schultz (2005), Evolution of damage zone geometry and intensity in porous sandstone: insight gained from strain energy density, *J. Geol. Soc.*, *162*(6), 939-949.

Olson, E.L., and M.L. Cooke (2005), Application of three fault growth criteria to the Puente Hills thrust system, Los Angeles, California, USA, *J. Struct. Geol.*, *27*(10), 1765-1777.

Park, J. O., T. Tsuru, Y. Kaneda, Y. Kono, S. Kodaira, N. Takahashi, & H. Kinoshita (1999). A subducting seamount beneath the Nankai accretionary prism off Shikoku, southwestern Japan. *Geophysical Research Letters*, *26*(7), 931-934.

Persson, K.S., and D. Sokoutis (2002), Analogue models of orogenic wedges controlled by erosion, *Tectonophysics, 356 (4)*, 323–336.

Pittarello, L., G. Di Toro, A. Bizzarri, G. Pennacchioni, J. Hadizadeh, and M. Cocco (2008), Energy partitioning during seismic slip in pseudotachylyte-bearing faults (Gole Larghe Fault, Adamello, Italy), *Earth Planet. Sci. Lett.*, *269*(1), 131-139.

Saffer, D. M., and B. A. Bekins (2002), Hydrologic controls on the morphology and mechanics of accretionary wedges, *Geology, 30*, 271– 274.

Savage, H.M., and M.L. Cooke (2010), Unlocking the effects of friction on fault damage zones. *J. Struct. Geol., 32 (11*), 1732-1741, doi:10.1016/j.jsg.2009.08.014.

Smit, J.H.W., J.P. Brun, and D. Sokoutis (2003), Deformation of brittle-ductile thrust wedges in experiments and nature, *J. Geophys. Res.: Solid Earth*, *108(B10).*

Souloumiac, P., Y.M. Leroy, B. Maillot, and K. Krabbenhøft (2009), Predicting stress distributions in fold-and-thrust belts and accretionary wedges by optimization, *J. Geophys. Res., 114*, doi:10.1029/2008JB005986.

Souloumiac, P., K. Krabbenhøft, Y.M. Leroy, and B. Maillot (2010), Failure in accretionary wedges with the maximum strength theorem: numerical algorithm and 2D validation, *Comput. Geosci., 14*, 793-811, doi:10.1007/s10596-010- 9184-4.

Souloumiac, Pauline; Maillot, Bertrand; Herbert, Justin W.; McBeck, Jessica A.; Cooke, Michele L. (2017): Supplement to "Work optimization predicts accretionary faulting: An integration of physical and numerical experiments". GFZ Data Services. http://doi.org/10.5880/fidgeo.2017.005

Souloumiac, P., B. Maillot, and Y. M. Leroy (2012), Bias due to side wall friction in sand box experiments, *J. Struct. Geol.*, *35*, 90-101, doi:10.1016/j.jsg.2011.11.002.

Storti, F., and K. McClay (1995), Influence of syntectonic sedimentation on thrust wedges in analog models, *Geology, 23*, 999 – 1002.

Takami, M. and T. Itaya (1996), Episodic accretion and metamorphism of Jurassic accretionary complex based on biostratigraphy and K-Ar geochronology in the western part of the Mino-Tanba Belt, Southwest Japan, *Island Arc, 5(3*), 321-336.

von Huene, R. and D.W. Scholl (1991), Observations at convergent margins concerning sediment subduction, subduction erosion, and the growth of continental crust, *Rev. of Geophys., 29(3*), 279-316.

Wang, K., & Hu, Y. (2006). Accretionary prisms in subduction earthquake cycles: The theory of dynamic Coulomb wedge. *Journal of Geophysical Research: Solid Earth*, *111*(B6).

Wenk, L. and K. Huhn (2013), The influence of an embedded viscoelastic–plastic layer on kinematics and mass transport pattern within accretionary wedges, *Tectonophysics, 608*, 653-666.

Willett, S. D. (1992), Dynamic and kinematic growth and change of a Coulomb wedge, in *Thrust Tectonics,* edited by McClay, pp. 19-31.

Wilson, B., T. Dewers, Z.E. Reches and J. Brune (2005), Particle size and energetics of gouge from earthquake rupture zones, *Nature*, *434*(*7034*), 749-752.

Xie, Y., & N. Kato, (2017). Fracture energies at the rupture nucleation points of large strike-slip earthquakes on the Xianshuihe fault, southwestern China. *Journal of Asian Earth Sciences*, *134*, 55-62.

Yamada, Y., K. Baba, A. Miyakawa and T. Matsuoka (2014), Granular experiments of thrust wedges: insights relevant to methane hydrate exploration at the Nankai accretionary prism, *Marine and Petroleum Geology, 51*, 34-48.

Yagupsky, D.L., B.A. Brooks, K.X. Whipple, C.C. Duncan, and M. Bevis (2014), Distribution of active faulting along orogenic wedges: minimum-work models and natural analogue, *J. Struct. Geol., 66*, 90–101, doi:10.1016/j.jsg.2014.05.025.

Yuan, X.P., B. Maillot, and Y.M. Leroy, (2015), Tectonic and gravity extensional collapses in overpressured cohesive and frictional wedges, *J. Geophys. Res*. *Solid Earth, 120,* doi:10.1002/2014JB011612.

Zhao, W. L., D. M. Davis, F. A. Dahlen, and J. Suppe (1986), Origin of convex accretionary wedges: Evidence from Barbados, *J. Geophys. Res., 91*, 10,246– 10,258.